ORIGINAL PAPER

A novel 3D train–bridge interaction model for monorail system considering nonlinear wheel-track slipping behavior

Yun Yang · Qinglie He · Chengbiao Cai · Shengyang Zhu · Wanming Zhai

Abstract Variable speed operation of the train cause easily the wheel-track slipping phenomenon, inducing strong nonlinear dynamic behavior of the suspended monorail train and bridge system (SMTBS), especially under an insufficient wheel-track friction coefficient. To investigate the coupled vibration features of the SMTBS under variable speed conditions, a novel 3D train–bridge interaction model for the monorail system considering nonlinear wheel-track slipping behavior is developed. Firstly, based on the D'Alembert principle, the vibration equations of the vehicle subsystem are derived by adequately considering the nonlinear interactive behavior among the vehicle components. Then, a high-efficiency modeling method for the large-scale bridge subsystem is proposed based on the component mode synthesis (CMS) method. The vehicle and bridge subsystems are coupled with a spatial wheel-track interaction model considering the nonlinear wheel-track sliding behavior. Furtherly, by a comprehensive comparison with the field test data, the effectiveness of the proposed method is verified, as well as the reasonable modal truncation frequencies of the bridge subsystem are determined. On this basis, the dynamics performances of the SMTBS are evaluated under different initial braking speeds and wheel-track interfacial adhesion conditions; besides, the nonlinear wheel-track slipping characteristics and their influences on the vehicle–bridge interaction are also revealed. The analysis results indicate that the proposed model is reliable for investigating the time-varying dynamic features of SMTBS under variable train speeds. Both the axle load transfer phenomenon and longitudinal slip of the driving tire would be easy to appear under the braking condition, which would significantly increase the longitudinal vehicle–bridge dynamic responses. To ensure a good vehicle–bridge dynamics performance, it is suggested that the wheel-track interfacial friction coefficient is larger than 0.35.

Keywords Suspended monorail · Vehicle–bridge interaction · Coupled vibration features · Wheel-track slipping behavior · Field test

1 Introduction

With the increase in urban traffic congestion and pollution, a variety of innovative transportation forms with new energy have been developed [1, 2], such as electric vehicles [3–5] and new-type rail transit systems [6], among which suspended monorail transportation (SMT) represents a promising alternative for alleviating such congestion due to its advantages including the strong climbing ability, small turning radius, low running noise [7]. At present, the SMT has

Y. Yang · Q. He (✉) · C. Cai · S. Zhu · W. Zhai
State Key Laboratory of Rail Transit Vehicle System,
Southwest Jiaotong University, Chengdu, China
e-mail: qlhe@swjtu.edu.cn

been mainly applied in Germany and Japan. In recent years, the SMT adopting new energy has been created in China [8–12], which has attracted extensive attention because of its remarkable advantages and the potential for integrating new technologies in the future [13–16].

In practical operating conditions, the suspended monorail train frequently experiences traction and braking due to numerous curved lines with small radius and large slope lines. Drastic fluctuations in train speed [17, 18] and inadequate adhesion conditions [19] could intensify the coupling vibration between the vehicle and bridge, thus reducing the stability of the vehicle and bridge, ride comfort for passengers, and even threatening the train running safety. Considering the large-scale thin-walled bridge structures [8], nonlinear wheel-track contact relationships [9], and strong nonlinear spatial coupling behavior between vehicle and bridge, the accurate modelling of the vehicle–bridge interaction (VBI) of SMT under variable speeds is a challenging research task. Therefore, to reveal the coupled vibration features of SMTBS induced by variable speed operation, it is particularly necessary to develop an efficient 3D train–bridge interaction model for SMTBS.

In the field of railway and highway transportation systems, the VBI has been a prominent research topic and many researchers have achieved significant breakthroughs [20, 21], such as theoretical modeling methodologies for the VBI [22], the effects of nonlinear parametric excitation [23] and nonlinear wheel-track contact behavior [24], evaluations of vehicle running safety [25], as well as developments in structural health monitoring with various equipment [26–30]. In contrast to the two systems mentioned above, the SMT possesses a unique vehicle–bridge system, in which the vehicle is suspended beneath a thin-walled box beam with an open bottom, as shown in Fig. 1. To reveal the vertical-lateral coupling features of VBI, Cai et al. [8] developed a two-dimension (2D) coupled dynamics model of the SMTBS based on the theory of multi-rigid body dynamics and finite element method (FEM). Jiang et al. [10] and Yang et al. [31] established a rigid-flexible coupling dynamics model by the Co-Simulation method, in which the main low-order modes of the guideway are reserved to simulate its flexibility. On this basis, many achievements have been made in

investigating coupled vibration characteristics of SMTBS under different track irregularity conditions [8, 12], selection of key parameters [9], as well as the effects of crosswind. Nevertheless, the existing methodologies primarily focus on studying vertical-lateral coupling features [8–10, 31] of the SMTBS, neglecting the longitudinal motion behavior and coupling effect between the vehicle elements. Nowadays, driving safely and favorable humanoid-assisted human interaction [32–36] have been very important and hot topics in SMT. To investigate the 3D dynamics features of SMTBS and ensure good operations (traction and braking), it is necessary to develop a 3D vehicle–bridge interaction model by further considering the longitudinal dynamic interaction. In terms of the bridge system, research [19] shows that the braking of a vehicle generates excitation forces that cover a wide range of frequencies, necessitating the utilization of numerous vibration modes or DOFs to accurately predict dynamic responses. The existing modeling methodologies of the SMT bridge subsystem mainly include FEM [8] and mode superposition method (MSM) [10], which mainly enable the investigation of the bridge dynamic responses in some typical bridge sections with a small scale. Once applied to the numerical solution or eigenproblem analysis of the large-scale bridge structures involving millions of DOFs, the two methodologies discussed above will require enormous computational resources. Therefore, to meet the requirements of the modeling of large-scale bridge structures, it is essential to develop a high-efficiency modeling method for the monorail bridge system.

The contact model between the tyres and the bridge surfaces poses another concern, typically employing a point contact model to ensure computational efficiency [37, 38]. Some researchers [39, 40] have found that the numerical model of VBI, which assumes the contact area as a point, lacks accuracy when considering road roughness. Besides, considering that the nonlinear stick–slip vibration of the tyre is highly dependent on the distribution of tyre normal forces [41] and wheel-track interfacial friction coefficients, the point contact model could fail to simulate this behavior. Especially for SMT, the thin-walled steel plate is designed as the running track, resulting in complex local deformation and a non-uniform distribution of normal load [8, 9]. Under variable speed conditions, the friction-induced wheel-track contact
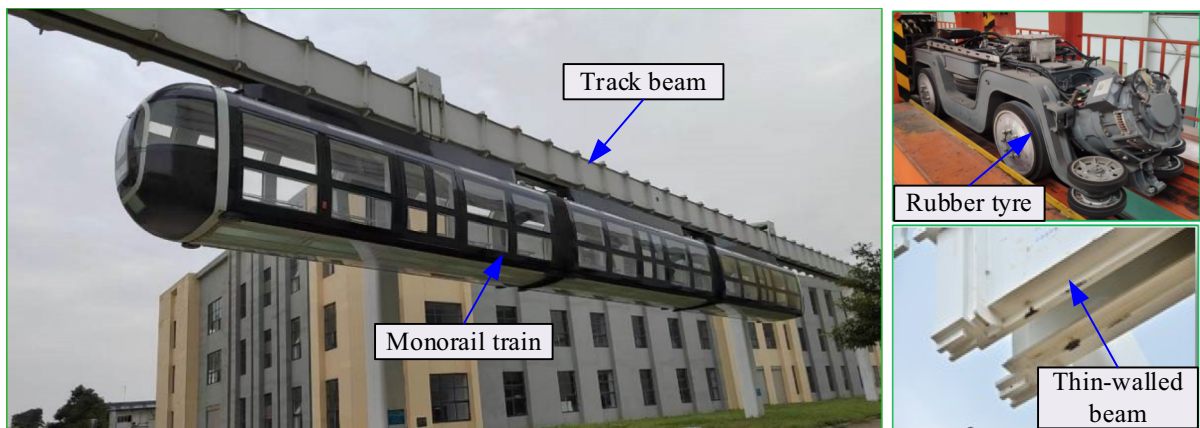
Fig. 1 Test line of the suspended monorail system in China

behavior of the SMTBS exhibits strong nonlinear features due to the significant discrepancies in the wheel structure, rubber material property, and wheel-track adhesion coefficients. Hence, a patch contact tyre model that incorporates the stick–slip vibration is essential for accurately simulating the spatial wheel-track nonlinear contact behavior. In the highway system, many mature tyre models have been developed and extensively applied, such as the Magic formula model [42], the Ftire model [43], the flexible ring model [44], and the FEM tyre model. The investigation of tyre mechanical properties commences with the pure cornering state and subsequently expands to encompass combined cornering, braking, and driving conditions [45]. However, the current tyre models are too complicated to be applied in vehicle–bridge dynamics simulation [46]. Besides, they are primarily utilized to research tyre and vehicle handling performances. Due to the significant coupling effects between the rubber tyre and thin-walled steel beam in SMTBS, the friction-induced nonlinear wheel-track slipping behavior is expected to have a more pronounced impact. Hence, it is necessary to develop a spatial wheel-track contact model of SMTBS and conduct a detailed investigation of VBI considering nonlinear wheel-track slipping behaviors.

To investigate the 3D coupled vibration features of the SMTBS under variable speed conditions, a novel 3D train–bridge interaction model considering nonlinear wheel-track slipping behavior is first developed and validated with the field test data in the present work. The main contributions are summarized as follows:

- The 3D coupled vibration equations of the vehicle subsystem of SMTBS are first derived by comprehensively considering the nonlinear interactive behaviour among its components.
- To simulate the nonlinear stick–slip vibration of the driving tyre reasonably, a simplified explicit wheel-track spatial contact model is developed by integrating the patch contact tyre model with the continuous radial multi-spring-damping element and the distributed LuGre friction model.
- To achieve high-efficiency and accurate dynamics simulation, a novel methodology for large-scale bridge modeling is proposed based on the CMS method and DMPF. The convergence and accuracy of the proposed method are discussed using the test data, and its modal truncation frequencies are recommended.

2 3D coupling dynamics model of the SMTBS

The section presents a novel 3D coupling dynamics model of the SMTBS, comprising the train subsystem, bridge subsystem, and a nonlinear wheel-track contact model. The train subsystem is modeled as a multi-rigid body system that considers the dynamic effects between the vehicle elements. The large-scale bridge subsystem is discretized as the periodic substructures, and its DOFs are effectively reduced by employing the CMS method. To model the nonlinear dynamic interaction between the driving tyre and the thin-walled track beam, a spatial wheel-track contact model considering nonlinear wheel-track stick–slip

behavior is developed. The detailed modeling methodologies will be elaborated in Sects. 2.1–2.3.

2.1 Train model

A monorail train is comprised of three locomotives connected by coupler and buffer systems and the suspension system is modeled with spring-damping elements. For each vehicle model, the car body, bogies, and center pins are all regarded as rigid-body with six DOFs, namely, longitudinal displacement X, lateral displacement Y, vertical displacement Z, roll angle φ, pitch angle β, and yaw angle Ψ, as shown in Fig. 2. The total DOFs of each vehicle are 38, as

shown in Table 1. The main assumptions of this model are summarized as follows:

Assumption 1 The four-linkage device is decoupled in the vertical and lateral by adopting two oblique springs, while its longitudinal mechanical behavior is represented by linear and torsional springs, enabling comprehensive 3D dynamics analysis of the train subsystem.

Assumption 2 Given that the driving tyres are connected to the bogie via the axles without the primary suspension, the pitching DOFs of the driving tyre are considered while other DOFs are coupled with the bogies.
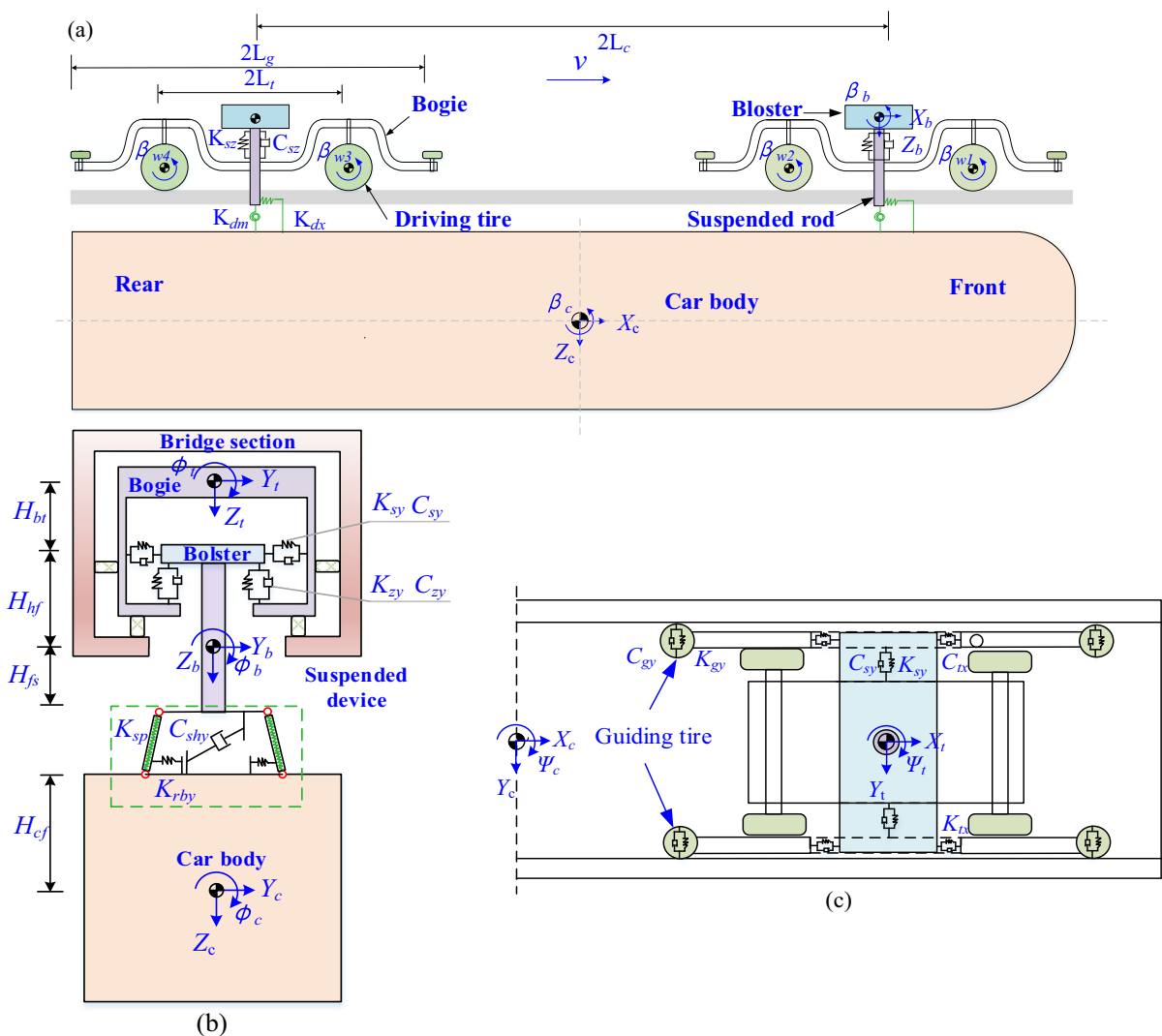
Fig. 2 Topological diagram of the vehicle structure: **a** Front view; **b** Left view; **c** Top view

Table 1 DOFs of the vehicle subsystem

Vehicle component	Longitudinal	Lateral	Vertical	Roll	Pitch	Yaw
Car body	X_c	Y_c	Z_c	Φ_c	β_c	Ψ_c
Bogie frame ($i = 1,2$)	X_{ti}	Y_{ti}	Z_{ti}	Φ_{ti}	β_{ti}	Ψ_{ti}
Hanging beam ($i = 1,2$)	X_{hi}	Y_{hi}	Z_{hi}	Φ_{hi}	β_{hi}	Ψ_{hi}
Wheelset ($i = 1$–4)	–	–	–	–	β_{wi}	–

2.1.1 Equations of motion

Based on the Newton–Euler method, the equations for the vehicle motion can be described as:

$$\begin{cases} \mathbf{M}_v\ddot{\mathbf{q}}_v = \mathbf{F}_{extv} + \mathbf{F}_{intv} \\ \mathbf{q}_v = \begin{bmatrix} \mathbf{q}_c\ \mathbf{q}_{b1}\ \mathbf{q}_{b2}\ \mathbf{q}_{t1}\ \mathbf{q}_{t2}\ \mathbf{q}_{w1}\ \mathbf{q}_{w2}\ \mathbf{q}_{w3}\ \mathbf{q}_{w4} \end{bmatrix}^T \end{cases} \quad (1)$$

where $\mathbf{M}_v$ is the mass matrix of the vehicle subsystem. $\mathbf{q}_v$ and $\ddot{\mathbf{q}}_v$ denote the displacement and acceleration vectors of the vehicle subsystem, respectively. The subscripts c, t, h, and w denote the car body, bogie, bolster, and driving tyre, respectively. $\mathbf{F}_{extv}$ denotes the external force vector of the train subsystem, which consists of the gravity force, the nonlinear force of the driving tyre and guiding tyre, traction/braking force, etc. $\mathbf{F}_{intv}$ denotes the internal force vector of the train subsystem, which can be obtained with the secondary suspension force, the force of the four-linkage suspended device, and the buffer force. The detailed components of the mass and force matrix can be referred to in Appendix A.

To investigate the 3D coupled vibration feature of the SMTBS, the eigenvalue analysis of the vehicle subsystem is carried out and the first several main vibration frequencies are listed in Table 2.

2.1.2 Four-linkage device decoupling

Noteworthily, to accurately model the coupled dynamics behavior between the components of the suspended monorail vehicle, it is imperative to effectively decouple its four-linkage device, as presented in Fig. 3a. In the authors' previous work [8], the four-linkage device is decoupled in the plane by adopting two oblique springs, which mainly allow for vibration analysis in vertical and lateral directions. On this basis, its longitudinal and pitching motion is decoupled with linear springs and torsion springs in this work, as illustrated in Fig. 3b, c.

Here, the coordinates vectors of the two ends of the oblique springs can be determined based on spatial coordinate transformation, and the force vectors $\mathbf{F}_{rod}$ can be expressed as:

$$\mathbf{F}_{rod} = \begin{bmatrix} F_{dx(u,p)i} \\ F_{dy(L,R)i} \\ F_{dz(L,R)i} \\ F_{d\beta(u,p)i} \end{bmatrix} = \begin{bmatrix} K_{dx}(X_{ci} - X_{hi} - H_{cb}\beta_{ci} - H_{hr}\beta_{hi}) \\ K_{spi}(\|\mathbf{r}_{pi} - \mathbf{r}_{ui}\| - l_o)\cos(\phi_{\pi i} - \phi_c) \\ K_{spi}(\|\mathbf{r}_{pi} - \mathbf{r}_{ui}\| - l_o)\sin(\phi_{\pi i} - \phi_c) \\ K_{dm}(\beta_{hi} - \beta_{ti}) \end{bmatrix} \quad (2)$$

where the subscripts 'u' and 'p' denote the upper and lower end of the four-linkage suspended device, respectively. l_0 is the length of the oblique springs. $\|\cdot\|$ is the second-moment norm of the vector. $F_{dx(u,p)i}$, $F_{dy(u,p)i}$, $F_{dz(u,p)i}$ and $F_{d\beta(u,p)i}$ are the longitudinal, lateral, vertical forces and pitching moment of the four-linkage device, respectively. $\mathbf{r}_{ui}$ and $\mathbf{r}_{pi}$ are spatial coordinate vectors for the upper and lower of the hinge joint, respectively, which can be written as:

Table 2 Main natural vibration frequencies of the vehicle

Mode	Frequency (Hz)	Motion of car body	Mode	Frequency (Hz)	Motion of bogie
1	0.357	Rolling	7	8.283	Rolling
2	1.650	Pitching	8	14.421	Vertical
3	1.690	Yawing	9	16.785	Lateral
4	1.950	Vertical	10	17.176	Pitching
5	2.390	Lateral	11	28.105	Yawing
6	4.080	Longitudinal	12	32.194	Longitudinal
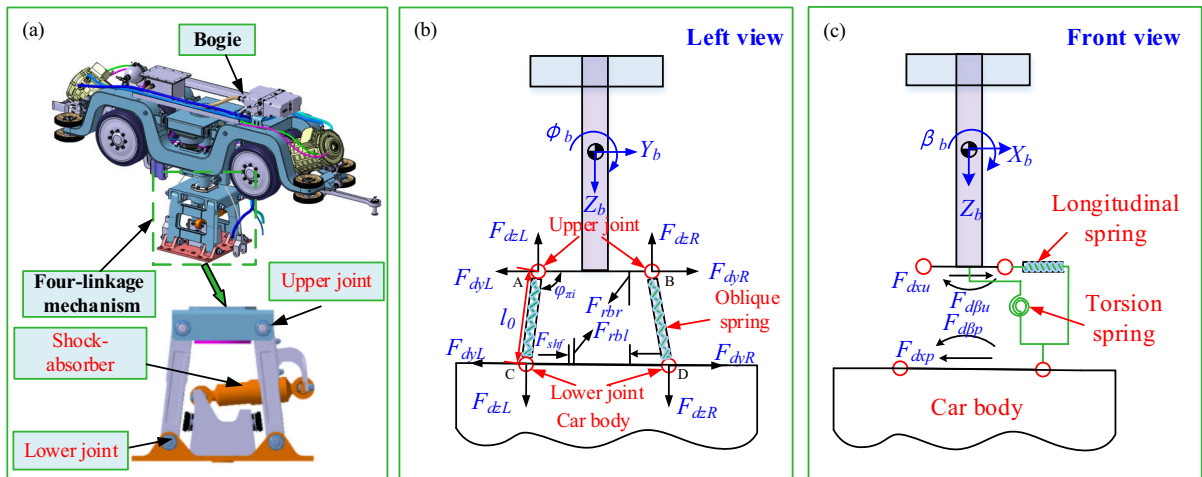
Fig. 3 The four-linkage mechanism schematic diagram: **a** Bogie and four-linkage mechanism; **b** Left view; **c** Front view

$$\mathbf{r}_{ui} = \mathbf{T}_{ui}\begin{bmatrix} y_{ov} \\ z_{ov} \end{bmatrix} + \begin{bmatrix} Y_{hi} \\ Z_{hi} - \mathrm{H}_{fs} \end{bmatrix},$$

$$\mathbf{r}_{pi} = \mathbf{T}_{pi}\begin{bmatrix} y_{ow} \\ z_{ow} \end{bmatrix} + \begin{bmatrix} Y_{ci} + s_1\Psi_{ci} \\ Z_{ci} - s_1\beta_{ci} - \mathrm{H}_{cf} \end{bmatrix} \tag{3}$$

where s_1 is the longitudinal distance from the car body centroid to the bogie centroid. (y_{ov}, z_{ov}) and (y_{ow}, z_{ow}) are the coordinates of the upper and lower of the hinge joint, respectively, $v = A, B$ and $w = C, D$. H_{cf} and H_{fs} are the vertical distances from the four-linkage device centroid to link AB and from the car body centroid to link CD, respectively. $\mathbf{T}_{ui}$ and $\mathbf{T}_{pi}$ are transformation matrices for the upper and lower of the hinge joint, respectively. The detailed spatial coordinate vectors can be referred to in Appendix A.

2.1.3 Coupler and buffer model

The coupler and buffer systems serve as crucial connecting components between the adjacent vehicles (refer to Fig. 4), playing a pivotal role in transmitting longitudinal force and mitigating longitudinal impact, particularly under varying speed conditions [20]. Considering time-varying relative speed and displacement between adjacent vehicles, the buffer force usually presents strong nonlinear features that can increase the longitudinal vibrations of the vehicles due to the dynamic interaction. A nonlinear spring-damping model is adopted to simulate the mechanical behavior of the coupler and buffer system of the

monorail vehicle, and its buffer force $\mathbf{F}_{\mathrm{cop}}(x, \Delta v)$ could be expressed as follows [20]:

$$\mathbf{F}_{cop}(x,\Delta v) = \begin{cases} 0.5[f_l(x)+f_u(x)]+0.5[f_l(x)-f_u(x)]\cdot\mathrm{sign}(\Delta v), |\Delta v| > v_f \\ 0.5[f_l(x)+f_u(x)]+0.5[f_l(x)-f_u(x)]\cdot\dfrac{\Delta v}{v_f}\cdot\mathrm{sign}(\Delta v), 0 < |\Delta v| < v_f \end{cases} \tag{4}$$

where $f_l(x)$ and $f_u(x)$ denote the loading and unloading forces of the buffer, respectively. Δv is the relative speed between adjacent vehicles. v_f is the switching speed between the loading and unloading conditions.

2.2 Nonlinear wheel-track spatial contact model

The SMT has a special wheel-track system, in which the rubber tyre runs on a thin-walled steel track. The thin-walled track may produce complex local deformation and vibration induced by moving vehicle loads, resulting in quite complicated wheel-track interaction features, especially under complex operating conditions (traction, braking, etc.), as shown in Fig. 5a. Considering that the nonlinear stick–slip vibration of the driving tyre is highly dependent on the distribution of normal forces and interfacial friction coefficient, a nonlinear wheel-track spatial contact model is developed by integrating the patch contact model and the extended distribution LuGre friction model [47, 48]. In this model, the non-uniformly distributed normal force could be modeled with the continuous radial multi-spring-damping element, as illustrated in Fig. 5b
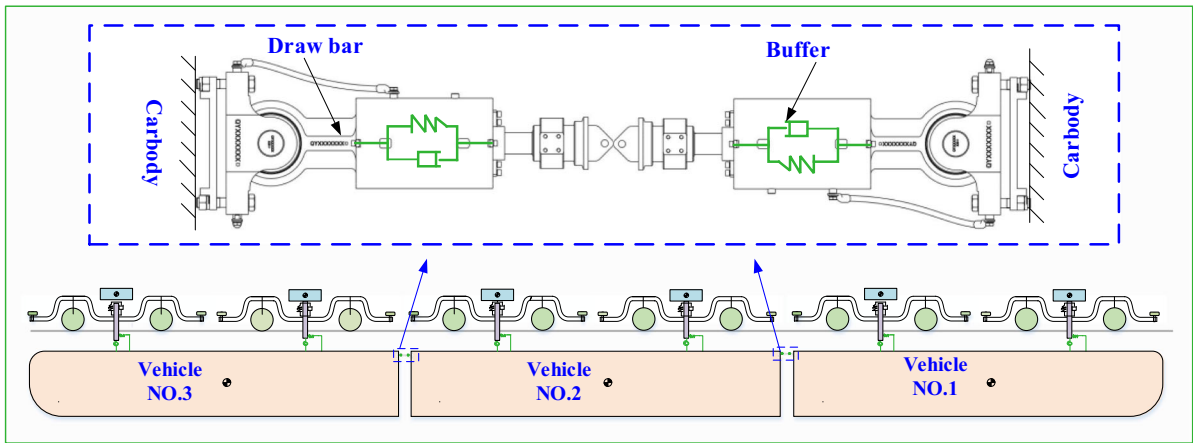
Fig. 4 Coupler and buffer model for monorail train
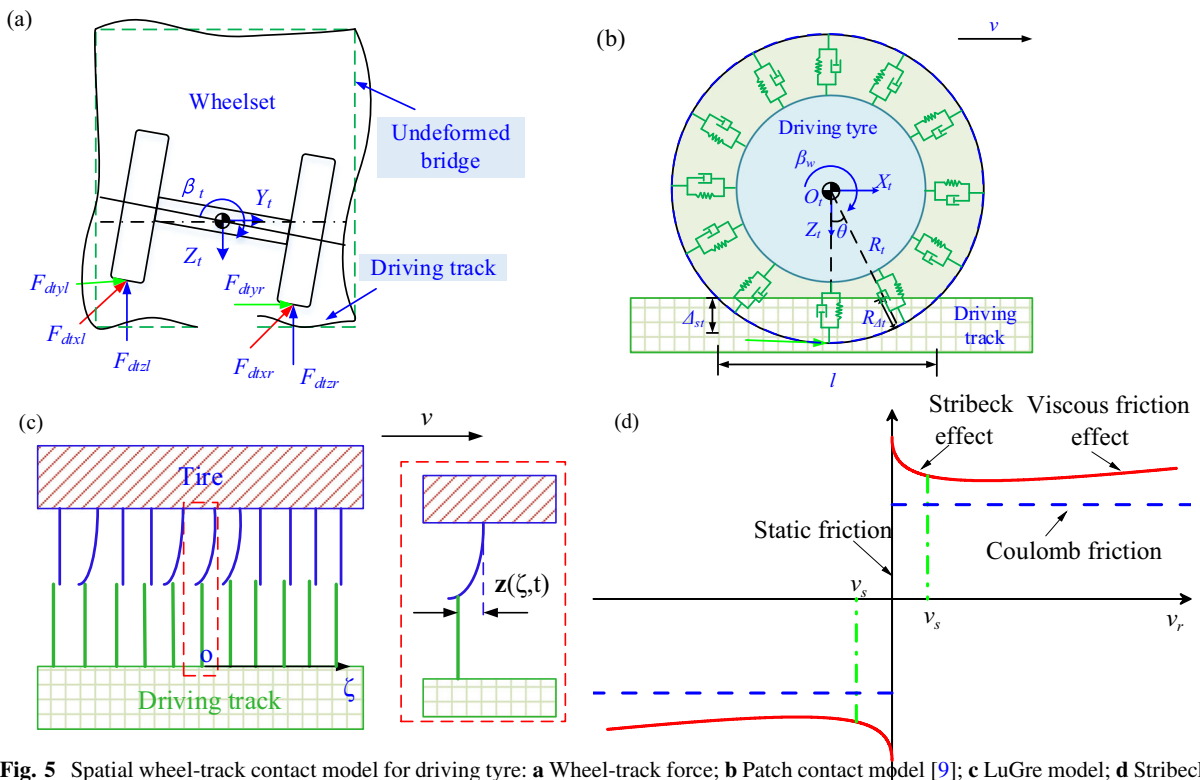
Fig. 5 Spatial wheel-track contact model for driving tyre: **a** Wheel-track force; **b** Patch contact model [9]; **c** LuGre model; **d** Stribeck effect

2.2.1 Wheel-track vertical force

As illustrated in Fig. 5a, considering the local deformation of the track deck, the vertical deformation $R_{\Delta dt}$ and corresponding change rate $\dot{R}_{\Delta dt}(\zeta, \tau)$ of the driving tyre in the contact region can be expressed as:

$$\begin{cases} R_{\Delta dt}(\zeta,\tau) = [Z_{ti} - s_3\beta_{ti} + (-1)^k b_4\varphi_{ti} - Z_b(\zeta,\tau) - Z_r + \Delta_{st} - R_t(1-\cos\theta)]/\cos\theta \\ \dot{R}_{\Delta dt}(\zeta,\tau) = [\dot{Z}_{ti} - s_3\dot{\beta}_{ti} + (-1)^k b_4\dot{\varphi}_{ti} - \dot{Z}_b(\zeta,\tau) - \dot{Z}_r + \Delta_{st} - R_t(1-\cos\theta)]/\cos\theta \end{cases}$$

(5)

where Z_b and Z_t represent the vertical displacements of the bridge and wheel, respectively. Z_r denotes the amplitude of track irregularity. Δ_{st} is the deformation

of the driving tyre under static load. θ is the angle between the contact point and the axle Z. ζ and τ are longitudinal and lateral coordinates in the coordinate system of the contact patch.

The normal contact behaviour of the driving tyre is simulated using the continuous radial multi-spring and damping element in Fig. 5b. The non-uniform distribution of normal forces can be described as [9]:

$$f_n(\zeta, \tau) = \begin{cases} (k_{dz}R_{\Delta dt}(\zeta, \tau) + c_{dz}\dot{R}_{\Delta dt}(\zeta, \tau))\cos\theta, & R_{\Delta dt} > 0 \\ 0, & R_{\Delta dt} \leq 0 \end{cases}$$
(6)

where k_{dz} and c_{dz} are radial stiffness and the damping of the driving tyre, respectively. The nonlinear radial stiffness and the equivalent viscoelastic damping of the driving tyre can be referred to [9].

Finally, the vertical force of the driving tyre can be obtained by integrating over the contact region:

$$F_{cdz} = \int_{-2/l}^{2/l} \int_0^b f_n(\zeta, \tau) d\zeta \, d\tau$$
(7)

where l and b are the length and width of the contact patch, respectively.

2.2.2 Wheel-track tangential force

Generally, the wheel-track tangential contact behaviour has a strong nonlinear feature, which depends on the adhesion condition and normal distribution force between the tyre and track. The LuGre friction model is adopted to compute the tangential forces that are affected by the normal contact force and relative tangential velocity between the tyre and track. In this model, the friction behaviour is considered as an interaction of the bristles between two surfaces, as illustrated in Fig. 5c. The distributed normalized friction force is determined by the deformation and the rate of brush bristle [47]:

$$\gamma(\zeta, t) = \boldsymbol{\sigma}_0 \mathbf{z}(\zeta, t) + \boldsymbol{\sigma}_1 \dot{\mathbf{z}}(\zeta, t) + \boldsymbol{\sigma}_2 \mathbf{v}_r$$
(8)

where $\boldsymbol{\sigma}_0 = [\sigma_{0x} 0; 0 \sigma_{0y}]$ is the stiffness of bristles. $\boldsymbol{\sigma}_1 = [\sigma_{1x} 0; 0 \sigma_{1y}]$ is the damping coefficient of brush bristle. $\boldsymbol{\sigma}_2 = [\sigma_{2x} 0; 0 \sigma_{2y}]$ is viscous friction coefficient of brush bristle. $\mathbf{z} = [z_x z_y]^T$ and $\dot{\mathbf{z}}(\zeta, t)$ are deformation and the rate of brush bristle, respectively. $\mathbf{v}_r$ is the slipping velocity.

To investigate the nonlinear stick–slip behavior between the wheel and track induced by different friction coefficients, the Stribeck effect is involved in this model, which could describe the negative slope relationship between the friction coefficient and the relative velocity, as illustrated in Fig. 5d. Hence, the internal friction states $\dot{\mathbf{z}}(\zeta, t)$ of the tyre on the contact patch and the transient function $g(\mathbf{v}_r)$ can be described as [47]:

$$\begin{cases} \dot{\mathbf{z}}(\zeta, t) = \mathbf{v}_r - \left(\dfrac{\boldsymbol{\sigma}_0 \mathbf{v}_r}{\mu_r g(\mathbf{v}_r)} - \kappa R_e |\omega| \right) \mathbf{z}(\zeta, t) \\ g(\mathbf{v}_r) = \dfrac{\|\boldsymbol{\mu}_c^2 \mathbf{v}_r\|}{\|\boldsymbol{\mu}_c \mathbf{v}_r\|} + \left(\dfrac{\|\boldsymbol{\mu}_s^2 \mathbf{v}_r\|}{\|\boldsymbol{\mu}_s \mathbf{v}_r\|} - \dfrac{\|\boldsymbol{\mu}_c^2 \mathbf{v}_r\|}{\|\boldsymbol{\mu}_c \mathbf{v}_r\|} \right) e^{-\|\mathbf{v}_r\|/v_s|^\alpha} \end{cases}$$
(9)

where $\boldsymbol{v}_r = [v_{rx} v_{ry}]^T$ and v_s denote the relative velocity between the driving tyre and the driving deck and Stribeck velocity, respectively. $\boldsymbol{\mu}_c = [\mu_{cx} 0; 0 \mu_{cy}]$ and $\boldsymbol{\mu}_s = [\mu_{sx} 0; 0 \mu_{sy}]$ denote the static friction coefficient and kinetic friction coefficient, respectively. $\|\cdot\|$ is the second-moment norm of the vector; α is the decay factor.

In Eq. (9), the wheel-track slipping behaviour depends on the relative velocity between the tyres and the track. The track beam will experience flexural and torsional composite deformation when subjected to vehicle loads, which has an important influence on the slipping behaviors of the driving tyres. The relative velocity between tyres and the track can be defined based on their kinematic relationship:

$$\begin{cases} v_{rx} = \omega R_e - \left[v_{tx} + (-1)^k b(\psi_t - \psi_b) \right] - v_{bx} \\ v_{ry} = v_{ty} - \left(\dot{\psi}_t L_w + \dot{\beta}_t h_w \right) - v_{by} \end{cases}$$
(10)

where v_{bx} and v_{by} are the longitudinal and lateral vibration velocities of the driving deck, respectively.

When $\dot{\mathbf{z}}(\zeta, t) = 0$ the steady-state solutions of the deformation of brush bristle can be obtained by integrating along the contact patch and the normalized friction force yields:

$$\begin{cases} \gamma_m(\zeta, t) = \lambda_{1m}(1 - \exp(-\zeta/\lambda_{2m})) \\ \lambda_{1m} = \text{sgn}(v_{rm})\dfrac{\mu g(v_{rm})}{\sigma_{0x}}; \lambda_{2m} = \left| \dfrac{\omega R_e}{v_{rm}} \right| \cdot \dfrac{\mu g(v_{rm})}{\sigma_{0x}} \end{cases}$$
(11)

where $m = x$ or y. x and y denote the longitudinal and lateral directions of the driving tyre, respectively.

Considering the distribution of normal load in Eq. (6), longitudinal force and lateral force of driving tyres can be expressed as:

$$F_{dtm} = \int_{-2/l}^{2/l} \int_0^b \gamma_m(\zeta, t) f_n(\zeta, \tau) d\zeta d\tau \qquad (12)$$

where F_{dtm} ($m = x$ or y) denotes the longitudinal force and lateral force. γ_m is the distributed normalized coefficient for tangential forces.

Additionally, the aligning moment of the driving tyre is also considered, which is defined as:

$$M_z = \int_{-2/l}^{2/l} \int_0^b \gamma_y(\zeta, t) f_n(\zeta, \tau)(L/2 - \zeta) d\zeta d\tau \qquad (13)$$

where γ_y is the distributed normalized coefficient for the lateral force.

2.3 Bridge model with the CMS method

To realize high-efficiency and accurate dynamics simulation, a novel methodology for large-scale bridge modeling is proposed based on the CMS method and DMPF. The main steps are presented as follows:

(1) First, the monorail bridge system is divided into multiple substructures, including the track beam and pier substructures. The kinetic energy and potential energy of the shell element are introduced into the Hamilton principle, and the mass and stiffness matrices of the shell element with 6 DOFs in each node can be obtained [49]. By assembling matrices of the shell element, the FE models of track beam and pier substructure are established, as shown in Fig. 6a, b.

(2) Further, by performing an eigenproblem analysis for each substructure separately, the corresponding eigenfrequencies and eigenmode matrixes could be obtained. Then, the reduced mass, stiffness, and mode shape matrixes can be obtained based on the Craig–Bampton method [50], in which the fixed-interfaced normal modes and constrained modes are combined as their reduced basis.

(3) Finally, a multi-span full-scale bridge subsystem could be reassembled by using the reduced track beam and pier submodels, in which the interface equilibrium conditions and compatibility conditions [51] of the interface nodes are adopted to connect the track beam and pier, as shown in Fig. 6c. On this basis, the equation of bridge motion could be established by further considering the Rayleigh damping [52].

2.3.1 Matrix formation and assembling of bridge substructures

2.3.1.1 Model reduction with the Craig–Bampton method In the CMS method, the stiffness and mass matrices of any substructure k are transformed as partitioned matrices according to the interface DOFs and internal DOFs. The governing equation of any undamped substructure k can be written as:

$$\begin{bmatrix} \mathbf{M}_{ii}^{(k)} \, sym. \\ \mathbf{M}_{bi}^{(k)} \, \mathbf{M}_{bb}^{(k)} \end{bmatrix} \begin{bmatrix} \ddot{\mathbf{u}}_i^{(k)} \\ \ddot{\mathbf{u}}_b^{(k)} \end{bmatrix} + \begin{bmatrix} \mathbf{K}_{ii}^{(k)} \, sym. \\ \mathbf{K}_{bi}^{(k)} \, \mathbf{K}_{bb}^{(k)} \end{bmatrix} \begin{bmatrix} \mathbf{u}_i^{(k)} \\ \mathbf{u}_b^{(k)} \end{bmatrix} = \begin{bmatrix} \mathbf{f}_i^{(k)} \\ \mathbf{f}_b^{(k)} \end{bmatrix} \qquad (14)$$

where $\mathbf{M}$, $\mathbf{C}$, and $\mathbf{K}$ denote the mass, damping, and stiffness matrices of each substructure, respectively. the symbols 'b' and 'i' denote the internal nodes and interface nodes, respectively. k is the kth substructure of the bridge and pier.

Based on the Craig–Bampton method, the transformation relationship from physical coordinate $\mathbf{u}^{(k)}$ to generalized coordinate $\mathbf{p}^{(k)}$ can be expressed as [39]:

$$\begin{bmatrix} \mathbf{u}_i^{(k)} \\ \mathbf{u}_b^{(k)} \end{bmatrix} = \mathbf{T}^{(k)} \begin{bmatrix} \mathbf{p}_i^{(k)} \\ \mathbf{p}_b^{(k)} \end{bmatrix} = \begin{bmatrix} \boldsymbol{\Phi}_{ir}^{(k)} & \boldsymbol{\Psi}_{ib}^{(k)} \\ \mathbf{0} & \mathbf{I}_{bb}^{(k)} \end{bmatrix} \begin{bmatrix} \mathbf{p}_i^{(k)} \\ \mathbf{p}_b^{(k)} \end{bmatrix} \qquad (15)$$

where $\boldsymbol{\Phi}_{ir}^{(k)}$ is the reserved fixed-interface normal mode with mass-normalized. $\boldsymbol{\Psi}_{ib}^{(k)}$ is the constrained mode. $\mathbf{I}_{bb}^{(k)}$ is the identity matrix.

To ensure the compatibility conditions of interfacial DOFs between each substructure, constrained modes are formed with the assumption that a unit displacement is imposed on one interface DOF and the other interface DOFs are fixed. This can be expressed as [39]:

$$\boldsymbol{\Psi}^{(k)} = \begin{bmatrix} -\left[\mathbf{K}_{ii}^{(k)}\right]^{-1} \mathbf{K}_{bb}^{(k)} \\ \mathbf{I}_{bb}^{(k)} \end{bmatrix} \qquad (16)$$
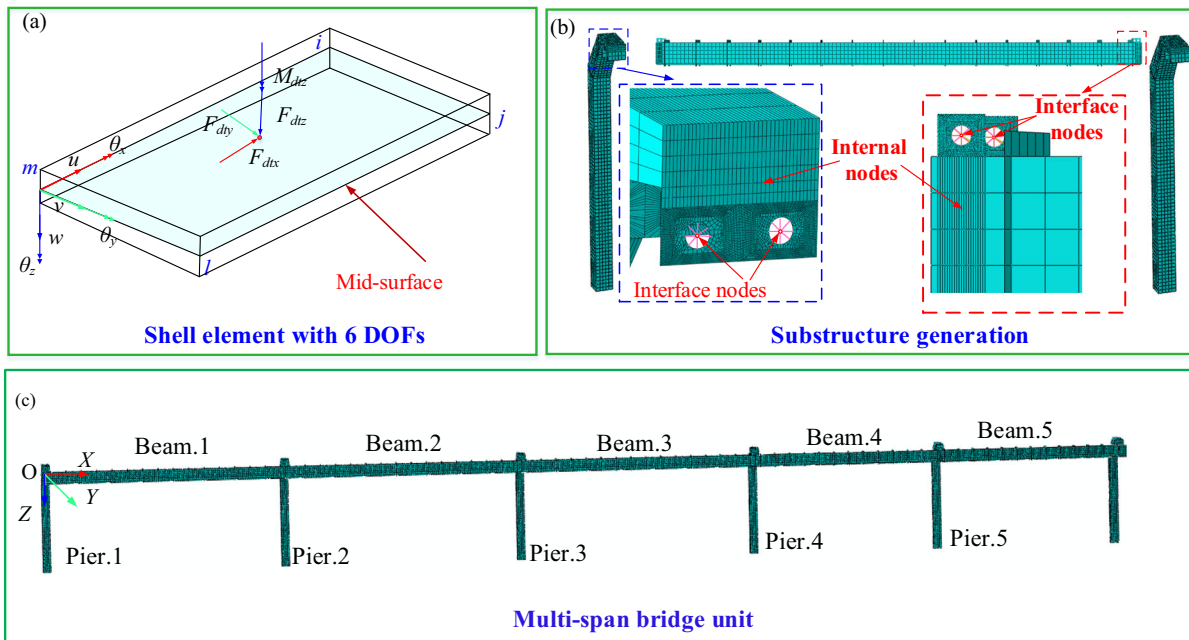
Fig. 6 The monorail bridge subsystem: **a** 4-node doubly curved thin or thick shell element; **b** 3D FEM of each substructure; **c** multi-span full-scale bridge subsystem

Furthermore, the reduced mass matrix and stiffness matrices of the kth substructure are formulated as follows:

$$\widetilde{\mathbf{M}}^{(k)} = \left(\mathbf{T}^{(k)}\right)^{\mathrm{T}}\mathbf{M}^{(k)}\mathbf{T}^{(k)}, \widetilde{\mathbf{K}}^{(k)} = \left(\mathbf{T}^{(k)}\right)^{T}\mathbf{K}^{(k)}\mathbf{T}^{(k)} \tag{17}$$

2.3.1.2 Matrix assembling of bridge subsystem In this research, not all the DOFs of interface nodes between the track beam and pier are compatible due to the simply supported constraint. The axis pins are modeled as a set of torsional springs in the rotational DOF θ_y and linear springs in the longitudinal DOF u_x, as shown in Fig. 7. Meanwhile, to reduce the interface DOFs, a set of hole nodes along the interface are coupled with a virtual center node (VCN) adopting multi-point constraints [53]. Hence, the DOFs of interface nodes above $\mathbf{u}_{bf} = [u^{\mathrm{VCN}}\ \theta_y^{\mathrm{VCN}}]$ are coupled only with force equilibrium conditions by torsional and linear springs while other DOFs $\mathbf{u}_{br} = [v^{\mathrm{VCN}}\ w^{\mathrm{VCN}}\ \theta x^{\mathrm{VCN}}\ \theta z^{\mathrm{VCN}}]$ are compatibility for the displacements and force equilibrium conditions. The bottom of the pier is fixed with the fixed constraint bolted connection.

To facilitate the analysis, all DOFs of the virtual node are divided into two categories: coupling with interaction forces (*F*DOFs) and coupling with displacements (*R*DOFs), as illustrated in Fig. 7. According to the classification of nodes above, the equation of motion of reduced substructure in Eq. (14) can be further partitioned as follows:

$$\begin{bmatrix} \widetilde{\mathbf{M}}_{ii}^{(k)} & \widetilde{\mathbf{M}}_{if}^{(k)} & \widetilde{\mathbf{M}}_{ir}^{(k)} \\ & \widetilde{\mathbf{M}}_{ff}^{(k)} & \widetilde{\mathbf{M}}_{fr}^{(k)} \\ sym & & \widetilde{\mathbf{M}}_{rr}^{(k)} \end{bmatrix} \begin{bmatrix} \ddot{\mathbf{p}}_i^{(k)} \\ \ddot{\mathbf{u}}_{bf}^{(k)} \\ \ddot{\mathbf{u}}_{br}^{(k)} \end{bmatrix}$$
$$+ \begin{bmatrix} \widetilde{\mathbf{K}}_{ii}^{(k)} & \widetilde{\mathbf{K}}_{if}^{(k)} & \widetilde{\mathbf{K}}_{ir}^{(k)} \\ & \widetilde{\mathbf{K}}_{ff}^{(k)} & \widetilde{\mathbf{K}}_{fr}^{(k)} \\ sym & & \widetilde{\mathbf{K}}_{rr}^{(k)} \end{bmatrix} \begin{bmatrix} \mathbf{p}_i^{(k)} \\ \mathbf{u}_{bf}^{(k)} \\ \mathbf{u}_{br}^{(k)} \end{bmatrix} = \begin{bmatrix} \mathbf{f}_i^{(k)} \\ \mathbf{f}_{\mathrm{int}}^{(k)} \\ \mathbf{f}_{br}^{(k)} \end{bmatrix} \tag{18}$$

where $\widetilde{\mathbf{M}}$ and $\widetilde{\mathbf{K}}$ denote reduced mass and stiffness matrices of the substructure, respectively. Symbols 'i', 'f', and 'r' denote the internal nodes, interface nodes coupling with force, and interface nodes coupling with displacement, respectively. Without loss of generality, the reduced basis $\mathbf{T}^{(k)}$ in Eq. (17) is also rewritten as:
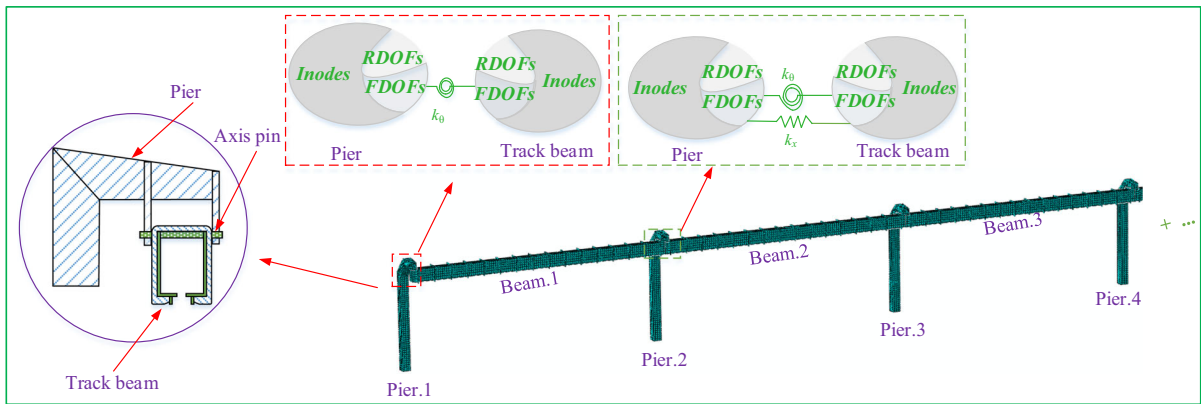
Fig. 7 Interface compatibility conditions of each substructure

$$\mathbf{T}^{(k)} = \begin{bmatrix} \mathbf{\Phi}^{(k)} & \mathbf{\Psi}^{(k)} \end{bmatrix} = \begin{bmatrix} \mathbf{\Phi}_{it}^{(k)} & \mathbf{\Psi}_{if}^{(k)} & \mathbf{\Psi}_{ir}^{(k)} \\ \mathbf{0} & \mathbf{I}_{ff}^{(k)} & \mathbf{0} \\ \mathbf{0} & \mathbf{0} & \mathbf{I}_{rr}^{(k)} \end{bmatrix} \quad (19)$$

where the constrained modes can be obtained with $\mathbf{\Psi}_{if}^{(k)} = -\left[\widetilde{\mathbf{K}}_{ii}^{(k)}\right]^{-1}\widetilde{\mathbf{K}}_{if}^{(k)}$ and $\mathbf{\Psi}_{ir}^{(k)} = -\left[\widetilde{\mathbf{K}}_{ii}^{(k)}\right]^{-1}\widetilde{\mathbf{K}}_{ir}^{(k)}$, respectively.

As shown in Fig. 6c, the full-size uncoupled bridge subsystem composed of m track beam and $m + 1$ piers is formulated by assembling the reduced mass and stiffness of the substructure, which can be obtained as:

$$\begin{cases} \mathbf{M}_b^e = blkdiag\left(\widetilde{\mathbf{M}}^{(p_1)}, \widetilde{\mathbf{M}}^{(b_1)}, \widetilde{\mathbf{M}}^{(p_2)}, \ldots, \widetilde{\mathbf{M}}^{(p_{(m+1)})}\right) \\ \mathbf{K}_b^e = blkdiag\left(\widetilde{\mathbf{K}}^{(p_1)}, \widetilde{\mathbf{K}}^{(b_1)}, \widetilde{\mathbf{K}}^{(p_2)}, \ldots, \widetilde{\mathbf{K}}^{(p_{(m+1)})}\right) \end{cases} \quad (20)$$

where $\widetilde{\mathbf{M}}^{(p_s)} \in \mathbb{R}^{n_{p_s} \times n_{p_s}}$ and $\widetilde{\mathbf{M}}^{(b_t)} \in \mathbb{R}^{n_{b_t} \times n_{b_t}}$ denote reduced mass matrices of the track beam and pier substructure, respectively. $\widetilde{\mathbf{K}}^{(p_s)} \in \mathbb{R}^{n_{p_s} \times n_{p_s}}$ and $\widetilde{\mathbf{K}}^{(b_t)} \in \mathbb{R}^{n_{b_t} \times n_{b_t}}$ denote reduced stiffness matrices of the track beam and pier substructure, respectively. $blockdiag\,(\cdot)$ denotes a block diagonal matrix.

The generalized coordinate $\mathbf{p} = \left[\mathbf{p}^{(p_1)}, \mathbf{u}^{(p_1)}, \mathbf{p}^{(b_1)}, \ldots, \mathbf{p}^{(p_{m+1})}, \mathbf{u}^{(p_{m+1})}\right]$ of the entire bridge subsystem is not independent due to some interface DOFs shared by multiple substructures. This can be transformed into a unique generalized coordinate $\mathbf{q} = \left[\mathbf{q}^{(p_1)}, \mathbf{q}^{(b_1)}, \mathbf{q}^{(p_2)}, \ldots, \mathbf{q}^{(p_{m+1})}\right]$ with a Boolean matrix $\mathbf{\Gamma}_B$. Hence, after the second reduction, the reduced matrices for the reassembled system yield:

$$\begin{cases} \widehat{\mathbf{M}}_b^e = (\mathbf{\Gamma}_B)^T \mathbf{M}_b^e \mathbf{\Gamma}_B \\ \widehat{\mathbf{K}}_b^e = (\mathbf{\Gamma}_B)^T \mathbf{K}_b^e \mathbf{\Gamma}_B \end{cases} \quad (21)$$

where $\mathbf{\Gamma}_B$ is a Boolean matrix and consists of elements 0 and 1. The matrix composition of $\mathbf{\Gamma}_B$ can be seen in Appendix B.

As mentioned above, each substructure is coupled by satisfying interface compatibility and equilibrium conditions. The governing equation of the entire bridge subsystem considering system damping could be further expressed as:

$$\widehat{\mathbf{M}}_b^c \ddot{\mathbf{q}}_b + \widehat{\mathbf{C}}_b^c \dot{\mathbf{q}}_b + \widehat{\mathbf{K}}_b^c \mathbf{q}_b = \mathbf{F}_i + \mathbf{F}_{\text{int}} \quad (22)$$

where $\mathbf{F}_i$ and $\mathbf{F}_{\text{int}}$ denote generalized external force and interface force vectors of the entire bridge subsystem, respectively. Interface force vector $\mathbf{F}_{\text{int}} = diag\left(\mathbf{f}_{\text{int}}^{(1)}, \mathbf{f}_{\text{int}}^{(2)}, \ldots, \mathbf{f}_{\text{int}}^{(n_{b_t})}\right)$, in which the interface forces of each substructure $\mathbf{f}_{\text{int}}^{(k)} = \left[f_{\text{int}1}^{(k)}, f_{\text{int}2}^{(k)}\right]^T$ can be written as follows:

$$\mathbf{f}_{\text{int}}^{(k)} = \begin{bmatrix} f_{\text{int}1\theta}^{(k)} \\ f_{\text{int}2x}^{(k)} \\ f_{\text{int}2\theta}^{(k)} \end{bmatrix} = \mathbf{k}_{\text{int}} \mathbf{u}_{bf}$$
$$= \begin{bmatrix} k_\theta & 0 & 0 \\ 0 & k_x & 0 \\ 0 & 0 & k_\theta \end{bmatrix} \begin{bmatrix} \theta_{y,VCN}^{(k)} - \theta_{y,VCN}^{(k-1)} \\ u_{x,VCN}^{(k+1)} - u_{x,VVN}^{(k)} \\ \theta_{y,VCN}^{(k+1)} - \theta_{y,VCN}^{(k)} \end{bmatrix} \quad (23)$$

where k_x and k_θ denote the stiffnesses of the torsional and longitudinal springs, respectively. f_{int1} and f_{int2} are the interaction forces at the left end and right end of the track beam, respectively.

Furthermore, the modal vectors of the reassembled reduced system are obtained with the Lanczos method [54] by solving the eigenproblem as follows:

$$(\widehat{\mathbf{K}}_b^c - \omega_r^c \widehat{\mathbf{M}}_b^c)\boldsymbol{\chi} = 0 \tag{24}$$

It is worth noting that the vector $\boldsymbol{\chi}$ has no practical meaning and is only the eigenvector of the reassembled system. The mode shape of the original model in physical coordinates is calculated by the multiplication of the vectors $\mathbf{T}^{(k)}\boldsymbol{\Gamma}_B\boldsymbol{\chi}$. For the convenience of description, $\varphi = \mathbf{T}^{(k)}\boldsymbol{\Gamma}_B\boldsymbol{\chi}$ is introduced.

2.3.2 Governing equation of the bridge

Due to the time-varying traction or braking force, wheel loads acting on the track deck should be determined with the time-varying velocity of each bogie. To obtain the dynamic responses of the track deck at any position and the time-varying dynamic interaction forces, the bilinear shape function $\mathbf{N}(t)$ for the 4-node isoparametric shell element is applied. The dynamic displacement and velocity of the bridge subsystem in physical coordinates could be expressed as:

$$\begin{cases} \mathbf{u} = \mathbf{N}(t)\mathbf{T}^{(k)}\boldsymbol{\Gamma}_B\boldsymbol{\chi}\mathbf{q} = \mathbf{N}(t)\varphi\mathbf{q} \\ \dot{\mathbf{u}} = \frac{\partial \mathbf{u}}{\partial t} + \frac{\partial \mathbf{u}}{\partial x}v = \mathbf{N}_s(t)\mathbf{T}^{(k)}\boldsymbol{\Gamma}_B\boldsymbol{\chi}\mathbf{q} + v\mathbf{N}(t)\mathbf{T}^{(k)}\boldsymbol{\Gamma}_B\boldsymbol{\chi}\mathbf{q} = \mathbf{N}_s(t)\varphi\mathbf{q} + v\mathbf{N}(t)\varphi\mathbf{q} \end{cases} \tag{25}$$

where $\mathbf{N}(t)$ and $\mathbf{N}_s(t)$ denote the shape function and the first derivative of the shape function with respect to coordinates for the shell element, respectively. These can be referred to in Appendix B.

The dynamic interaction forces will be assigned to each node d ($d = i, j, k, m$) adopting the shape function $\mathbf{N}(t)$, as illustrated in Fig. 6a. Furthermore, the generalized force matrix $\mathbf{P}_b$ of distributed normal force acting on the node of the track deck can be transformed with:

$$\begin{cases} \mathbf{f}_d = \sum_j^{n=8} \iint_s \mathbf{N}(t)\varphi_j^d (f_n(\zeta,\tau)d\zeta d\tau) - \mathbf{F}_{vg}(t) \\ \mathbf{f}_g = \sum_j^{n=8} \iint_s \mathbf{N}(t)\varphi_j^g \mathbf{F}_{int}(t) \\ \mathbf{P}_b = \mathbf{f}_d + \mathbf{f}_g \end{cases} \tag{26}$$

where $\mathbf{P}_b$ denotes the matrix of generalized external force. $\mathbf{f}_d$ and $\mathbf{f}_g$ denote the generalized force matrices of driving and guiding tyres, respectively. $\mathbf{F}_{intb} = \begin{bmatrix} \mathbf{F}_{dtx}, \mathbf{F}_{dty}, \mathbf{F}_{dtz}, \mathbf{0}, \mathbf{0}, \mathbf{M}_{dtz} \end{bmatrix}$ and $\mathbf{F}_{intg} = \begin{bmatrix} \mathbf{F}_{gx}, \mathbf{F}_{gv}, \mathbf{0}, \mathbf{0}, \mathbf{0}, \mathbf{0} \end{bmatrix}$ denote the nonlinear forces of the driving tyre and guiding tyre, respectively.

Based on the analysis above, the time-varying governing equation for the bridge subsystem considering system damping could be further expressed as:

$$\overline{\mathbf{M}}_b^c \ddot{\mathbf{q}}_b + \overline{\mathbf{C}}_b^c \dot{\mathbf{q}}_b + \overline{\mathbf{K}}_b^c \mathbf{q}_b = \mathbf{P}_b + \mathbf{F}_{intb} \tag{27}$$

where $\mathbf{P}_b$ and $\mathbf{F}_{intb}$ denote the matrices of generalized external force and interaction force, respectively. $\overline{\mathbf{M}}_b^c = \mathbf{N}(t)\varphi(t)\mathbf{M}_b$; $\overline{\mathbf{K}}_b^c = \mathbf{N}(t)\varphi(t)\mathbf{K}_b$; $\overline{\mathbf{C}}_b^c = \mathbf{N}(t)\varphi(t)\mathbf{C}_b$; $\mathbf{F}_{intb} = \varphi\mathbf{F}_{int}$. $\mathbf{C}_b$ can be obtained with the Rayleigh-damping based on the equation $\mathbf{C}_b = \alpha\mathbf{M}_b + \beta\mathbf{K}_b$ referred to in the literature [52].

2.3.3 Determination of the modal truncation frequencies

The modal truncation frequencies have a crucial influence on the simulation accuracy of the bridge model in the CMS method. Generally, the contribution of a certain vibration mode in the total dynamic responses of the structure is evaluated utilizing the modal participation factors (MPF), which are usually defined with the mass matrix form [55, 56]. This method only could consider the inherent properties of the structure, neglecting the structural dynamic interaction effect. However, for the vehicle–bridge system with time-varying features, both the loading frequency and spatial mass distribution of the moving vehicle would have important influences on the modal contributions of the bridge.

To determine a reasonable modal truncation number (MTN) involving the influences of VBI and the random excitation of track irregularity, a more effective dynamic modal participation factor (DMPF) is defined. Taking the vibration acceleration of the bridge as an example, the DMPF (Γ_{pi}) of vibration mode i is defined as:

$$\Gamma_{pi} = \begin{cases} \dfrac{rms(\varphi_i^{kt}\ddot{q}_i(t))}{rms(\ddot{\mathbf{u}}_b^{kt}(t))} \\ \dfrac{\max(\varphi_i^{kt}\ddot{q}_i(t))}{\max(\ddot{\mathbf{u}}_b^{kt}(t))} \end{cases} \tag{28}$$

where φ_i^{kt} and $\ddot{q}_i(t)$ denote the modal shape vector at node kt and acceleration modal coordinate in time step t of vibration mode i, respectively. $\ddot{\mathbf{u}}_b^{kt}(t)$ is the dynamic response of the bridge subsystem in node kt. rms$(\cdot)$ and max$(\cdot)$ denote the operation calculating the root mean square value and maximum value, respectively.

The convergence criterion for the dynamic responses of the bridge subsystem is defined as:

$$\begin{cases} \sum \Gamma_{pi} > \eta_{sum} \\ \Delta\Gamma_{pi} < \eta_\Delta \end{cases} \tag{29}$$

where η_{sum} and η_Δ denote the threshold value of accumulated contribution participation and the difference of DMPF between the ith mode and $i + 1$th mode, respectively. When η_{sum} is close to 1 and η_Δ is small enough, the MTN is determined.

2.4 Modelling of three-dimensional train–bridge interaction

In terms of a time-varying coupled system, the governing equations of the vehicle–bridge system can be written as:

$$\mathbf{M}(t)\mathbf{q} + \mathbf{C}(t)\dot{\mathbf{q}} + \mathbf{K}(t)\mathbf{q} = \mathbf{F}(t) \tag{30}$$

where

$$\mathbf{M} = \begin{bmatrix} \mathbf{M}_v & \mathbf{0} \\ \mathbf{0} & \overline{\mathbf{M}}_b^c \end{bmatrix}, \mathbf{C} = \begin{bmatrix} \mathbf{C}_{vv} & \mathbf{0} \\ \mathbf{0} & \overline{\mathbf{C}}_{bb} \end{bmatrix}, \mathbf{K} = \begin{bmatrix} \mathbf{K}_{vv} & \mathbf{0} \\ \mathbf{0} & \overline{\mathbf{K}}_{bb} \end{bmatrix},$$

$$\mathbf{q} = \begin{bmatrix} \mathbf{q}_v \\ \mathbf{q}_b \end{bmatrix}, \mathbf{F} = \begin{bmatrix} \mathbf{F}_{extv} + \mathbf{F}_{intv} \\ \mathbf{P}_b + \mathbf{F}_{intb} \end{bmatrix} \tag{31a}$$

$$\begin{cases} \mathbf{M}_v = \mathbf{M}_v \\ \overline{\mathbf{M}}_b^c = \mathbf{N}(t)\boldsymbol{\varphi}(t)\mathbf{M}_b \end{cases}, \begin{cases} \mathbf{C}_{vv} = \mathbf{C}_v \\ \overline{\mathbf{C}}_{bb} = \mathbf{N}(t)\boldsymbol{\varphi}(t)\mathbf{C}_b \end{cases},$$

$$\begin{cases} \mathbf{K}_{vv} = \mathbf{K}_{vv} \\ \overline{\mathbf{K}}_{bb} = \mathbf{N}(t)\boldsymbol{\varphi}(t)\mathbf{K}_b + v\mathbf{C}_b\mathbf{N}_s(t)\boldsymbol{\varphi}(t) \end{cases} \tag{31b}$$

where $\mathbf{M}$, $\mathbf{C}$, and $\mathbf{K}$ denote the mass, damping, and stiffness matrices for the SMTBS, respectively; $\mathbf{F}$ denotes the force matrix including the dynamic interaction force and the gravity; the subscripts v and b represent the vehicle and the bridge subsystem, respectively.

Noteworthily, the motion equations of the vehicle subsystem, bridge vibration equations with the CMS method, and nonlinear spatial wheel-track contact relation are all programmed applying the software MATLAB® in this work, in which the vehicle dynamics responses are solved with the Zhai method [57] and the bridge dynamic responses with the Newmark-β method [58]. The main steps and flow chart of this work are illustrated in Fig. 8.

3 Model verification

In this section, a full-scale field test is conducted to verify the effectiveness of the proposed coupling dynamic model, and its convergence is also carefully discussed.

3.1 Full-scale field test

The full-scale field test is carried out to obtain the coupled dynamic responses of the SMTBS based on the first test line in Chengdu, China. In this test line, the experimental train consists of three vehicles, and the test bridge is multi-span simply supported beams with hollow piers. To obtain the vehicle–bridge accelerations, several wireless triaxial accelerometers are used to measure the vibrations of the vehicle and bridge in longitudinal, lateral, and vertical directions. The sampling frequency is set as 5000 Hz. Additionally, the mid-span deformation of the bridge is tested by an advanced displacement test instrument (ADTI).

As shown in Fig. 9, the setting positions of the acceleration sensor and target for displacement are presented clearly, respectively. The triaxial accelerometers are placed on the floor of the car body according to the standard [59], as shown in Fig. 9a. For the bridge subsystem, the triaxial accelerometers are placed on the bottom of the track beam while the observation point of the displacement is set at the center of the track beam, as shown in Fig. 9b, c.

3.2 Modal verification

The main vibration frequencies and modal shapes derived from the CMS method and FEM are compared with those of the previous field test [8], as shown in Table 3 and Fig. 10. One can observe that the main frequencies and modal shapes obtained from the proposed method are consistent with those of the traditional FEM. Besides, the simulation results based on the two methods are close to the test results [8],
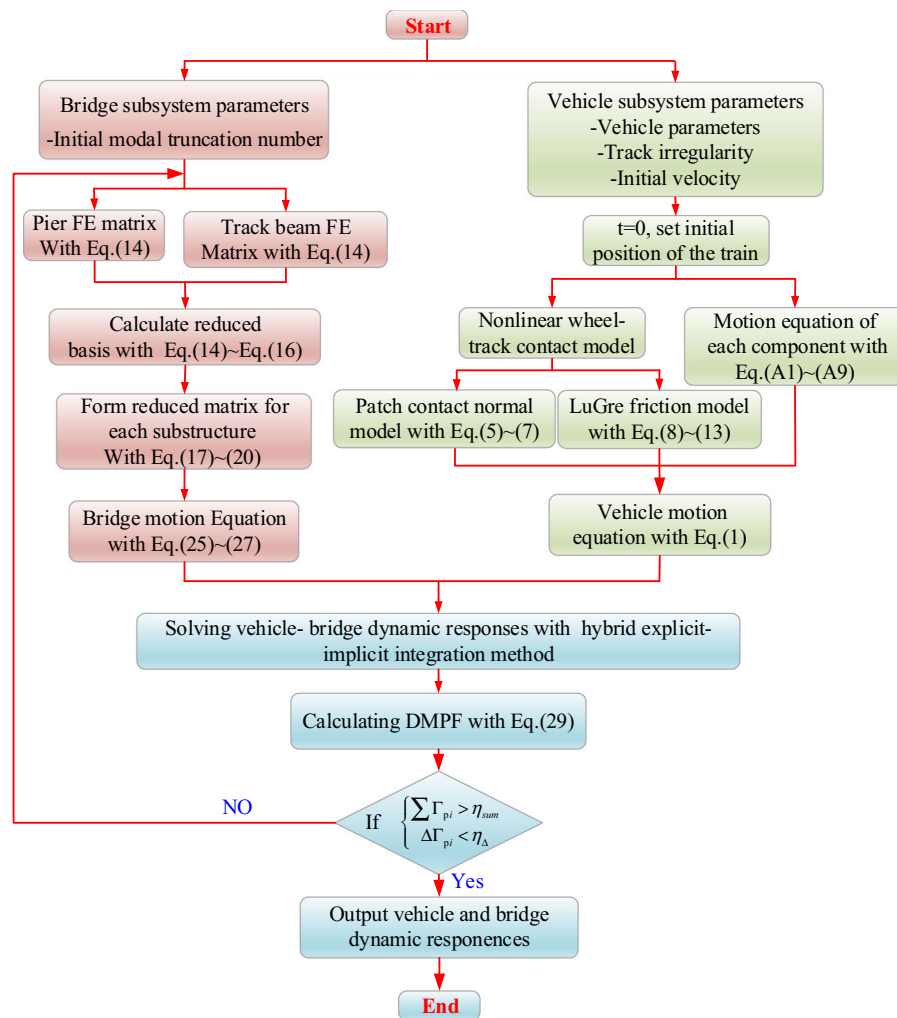
Fig. 8 Flow chart and main step of the proposed 3D train–bridge interaction model

indicating the reliability and accuracy of the proposed method.

3.3 Selection of the modal truncation frequencies of the bridge

The impact of track irregularity and loading moving frequencies on the VBI is significant. To address this issue, the contribution of each mode is analyzed under the disturbance of track irregularity and different loading moving frequencies by adopting the DMPF (Eq. (28)), as illustrated in Fig. 11. The track irregularity adopts the measured result referred to [8].

As can be seen in Fig. 11a, compared with the case without the random track irregularity, the DMPFs of

the bridge modes under the random track irregularity are significantly different, especially at several main frequency ranges of 3.5–7.0 Hz, 11.0–16.0 Hz, and 17.5–18.9 Hz, respectively. It is indicated that the track irregularity would stimulate the bridge vibrations at different frequency bands, thus affecting the contribution of each bridge mode to the vibration responses. Further, to explore the effects of the loading moving frequency, the DMPFs under different speeds are compared, as can be seen from Fig. 11b. Clear discrepancies can be observed in the range of 4.1–7.1 Hz and 10.9–16.3 Hz, which are mainly induced by the wheelbase (L_c = 1.6 m) and stronger dynamic effect due to the increase in velocity, respectively. It could be concluded that both the track
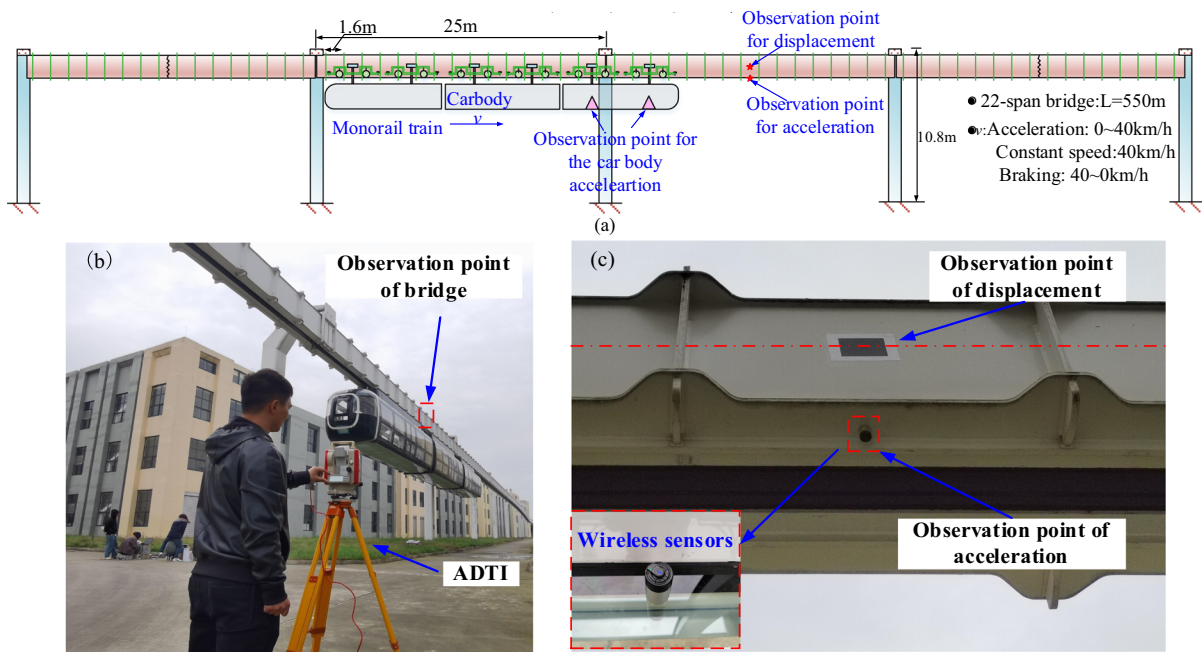
Fig. 9 Vehicle–bridge interaction model and sensors arrangement in the field test: **a** Sensors arrangement; **b** ADTI; **c** the observation point of track beam

Table 3 Main natural frequencies of the bridge

Modal order	Modal shape	Symbol	CMS (Hz)	FEM(Hz)	Test results (Hz)
1	Longitudinal vibration of the bridge	f_{bll}	1.95	1.94	–
2	1st coupled lateral-and-torsional vibration	f_{bl1}	2.34	2.34	2.27 [8]
3	Lateral bending vibration of the pier	f_{pl}	3.33	3.33	–
4	1st vertical bending vibration	f_{bv1}	5.43	5.44	5.60 [8]
5	2nd coupled lateral-and-torsional vibration	f_{bl2}	9.13	9.14	9.55 [8]
6	2nd vertical bending vibration	f_{bv2}	15.92	15.92	15.19 [8]

irregularity disturbance and loading moving frequency should be adequately considered in the selection of the bridge MTN. Besides, these results also reveal the importance of considering the VBI to some extent and highlight the necessity of the DMPF.

Next, a case study of determining MTN based on DMPF is presented when the monorail train travels through the bridge at a constant speed of 40 km/h. The first 200 modes of the bridge are reserved at the beginning and the specific value of MTN is determined according to the convergence criterion in Eq. (29), as shown in Fig. 12.

The accumulated DMPF of the displacements and accelerations in longitudinal, lateral and vertical directions are illustrated in Fig. 12. According to the convergence criterion in Eq. (29), when the accumulated DMPF is close to 1, the extracted bridge modes would be reasonable. As depicted in Fig. 12a, the MTN of the longitudinal, lateral, and vertical displacements should be up to 67, 56, and 108 respectively for ensuring a high simulation accuracy. According to Fig. 12b, the minimum required MTN for longitudinal, lateral, and vertical acceleration is 179, 186, and 188 respectively. The results indicate that it is necessary to extract more modal orders of the
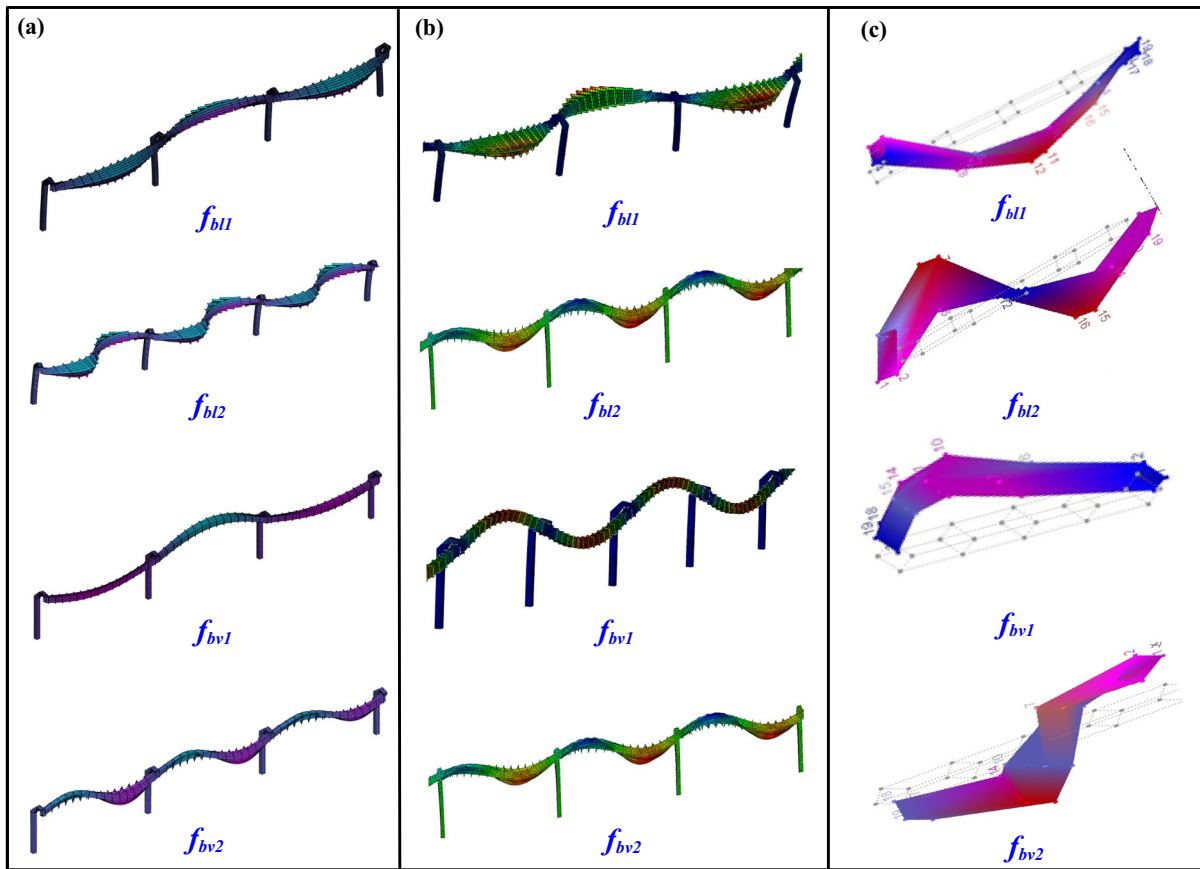
Fig. 10 Modal comparison between simulation and field test: **a** Proposed method; **b** FEM; **c** Field test [8]

bridge to ensure the convergence of bridge acceleration. Hence, based on the convergence criterion in Eq. (29), the MTN is 188 at least for guaranteeing the accuracy of the bridge dynamic responses.

3.4 Verification of vehicle–bridge dynamic responses under variable speed

The vehicle–bridge dynamic responses obtained from the simulation model are compared with those of the field test under a complex operating condition encompassing the complete running process of vehicle acceleration, constant speed, and braking.

3.4.1 Vehicle dynamic responses

In this case, the traction or braking torque is exerted on the wheels and the curves are depicted in Fig. 13. In this simulation, the track irregularity is referred to [8] and the main calculation parameters of the monorail

train and bridge are listed in Table 4 and Appendix C. The bridge model is composed of 22 span track beams with a total length of 550 m, whose MTN is 200 based on the proposed DMPF. Based on this, the time-domain responses of the car body obtained by the simulation and test are compared when the vehicle accelerates from 5 km/h to 40 km/h first and then decelerates to 0 km/h, as shown in Fig. 14.

As shown in Fig. 14, the waveform and amplitudes of the vehicle accelerations in each direction obtained from the simulation are well consistent with those of the test data under constant and variable speeds, indicating the reliability of the proposed model. Moreover, it could be observed that the lateral and vertical accelerations of the car body gradually increase when the running speed rises from 5 to 40 km/h. Subsequently, it would gradually decrease when the running speed reduces from 40 km/h to 0. In particular, regarding the longitudinal vibration of the car body, Fig. 14a shows a sudden enlargement of the
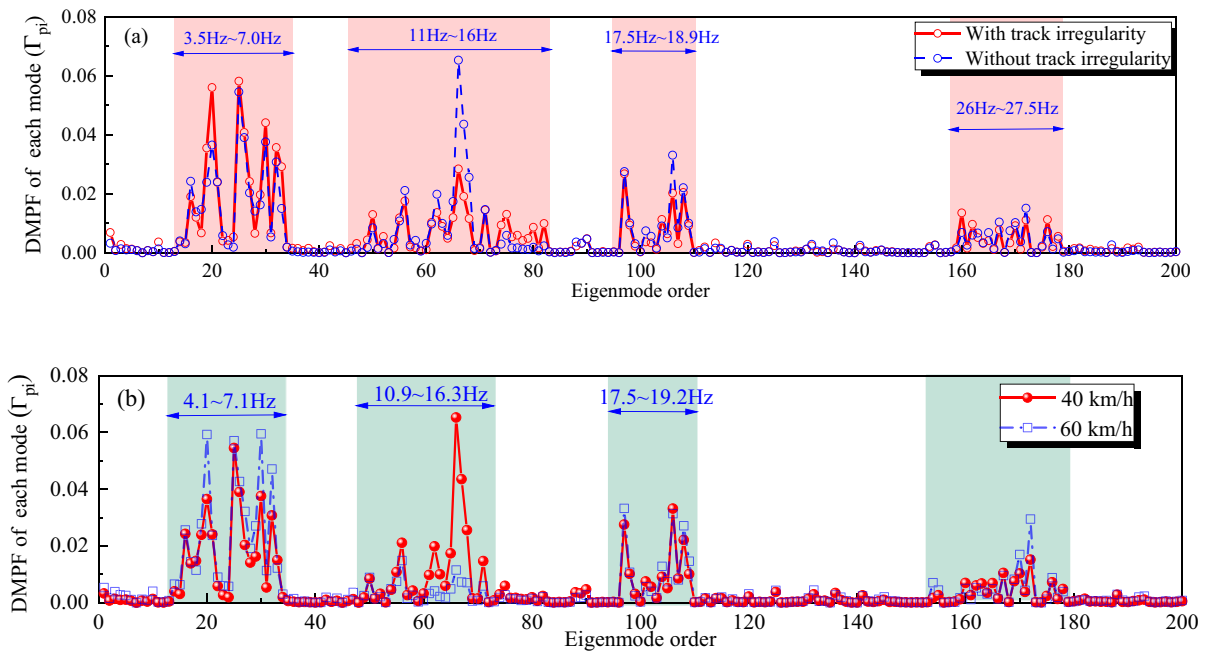
Fig. 11 Contribution participation considering the VBI under different excitations: **a** Track irregularity; **b** Running speed
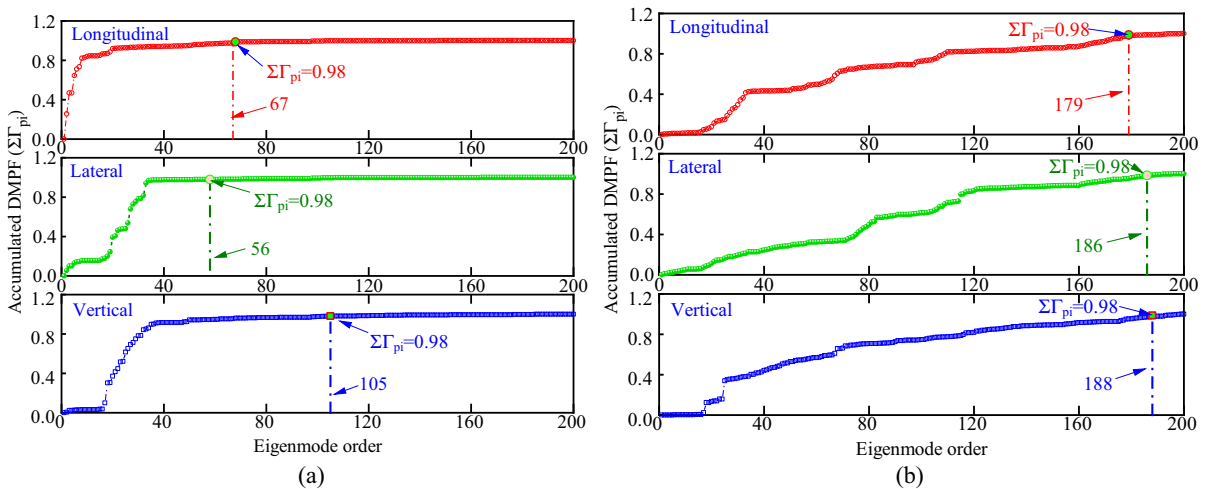
Fig. 12 DMPF of each mode: **a** DMPF of the displacement; **b** DMPF of the acceleration

vibration at the initial braking position (at the 30 s). Simultaneously, the vertical acceleration of the car body exhibits a significant peak value, which may be attributed to the sudden increase in braking forces. Besides, the car body will appear oscillatory due to the inertia force when the braking force decreases to 0 at the braking ending position (at the 38 s). However, these oscillations dissipate within a duration of around 3 s.

To reveal the time-varying features of the vehicle vibration frequency under variable speed conditions, the time–frequency responses of the car body accelerations obtained from simulation and test results using the continuous wavelet transform method [60] are compared, as depicted in Fig. 15.

It could be seen from Fig. 16 that the pitching motion frequency f_{vp} (1.65 Hz), lateral motion frequency f_{vl} (2.39 Hz), and vertical motion frequency f_{vv}

(1.95 Hz) of the car body identified from the simulation and test results have time-varying features due to vehicle–bridge interaction. Additionally, one can observe that the loading frequencies f_1 and f_2 change as the variable train running speeds, in which the f_1 is induced by the span of the track beam ($L_B = 25.0$ m), and the f_2 is the double frequency multiplication of the f_1. A similar phenomenon can also be observed from the loading frequencies f_3 and f_4, which are induced by the wheelbase ($L_c = 1.6$ m) and the space of the stiffener ($L_s = 1.6$ m). The abovementioned results indicate that the simulation results derived from the proposed model are consistent with the test results at the main frequency bands. Simultaneously, the time-varying coupling features of the SMTBS under variable speed conditions could be also simulated effectively with the proposed models.

3.4.2 Bridge dynamic responses

To verify the accuracy of the bridge dynamic responses obtained from the proposed method, the dynamics simulation results based on the CMS method and FEM are compared with the field test results when monorail trains travel through the bridge at a constant speed of 40 km/h, as depicted in Figs. 16 and 17.

As shown in Figs. 16 and 17, the waveform and peak of the bridge displacements and accelerations obtained by the numerical simulation are in good

agreement with the test data in time domains. The maximum relative error of vertical and lateral displacement between the simulation and measured results are only 1.9 and 3.2%, respectively. It could be also observed that the maximum values of bridge acceleration in longitudinal, lateral, and vertical directions are about 0.054, 0.30, and 0.21 g, respectively, which means that the monorail bridge has stronger vibration in the lateral direction due to its small lateral bending stiffness. Additionally, the comparison of computational time between the proposed method and the traditional FEM is presented in Table 5. It can be seen that the computational time of the proposed method is about 1/5 of the traditional FEM while almost similar accuracy is achieved. It indicates that the proposed method based on CMS has higher computational efficiency and accepted computational accuracy.

The time–frequency distributions comparison of bridge accelerations between the proposed model and field test is illustrated in Fig. 18.

Some characteristic frequencies of the dynamics system can be identified in the time–frequency responses. Besides, it can be observed that the load frequencies and natural frequencies of the bridge subsystem obtained from the simulation and field test results are also very close. Taking the vertical acceleration as an example, the load frequency f_1 induced by the span of the bridge ($L_B = 25$ m) observed from the simulation and field test results are 0.45 and 0.42 Hz, respectively. Similarly, the loading frequency f_3 induced by the wheelbase ($L_c = 1.6$ m) obtained from the simulation and test results are 6.94 and 6.95 Hz, respectively. As for the bridge frequencies, the first bending vibrations frequency f_{bv1} observed from the simulation and test results are 5.43 and 5.65 Hz, respectively. Meanwhile, the lateral bending vibration frequency f_{pl} of the pier observed from the simulation and test results are both 3.33 Hz. Additionally, analogous results can be seen in longitudinal and lateral accelerations. The
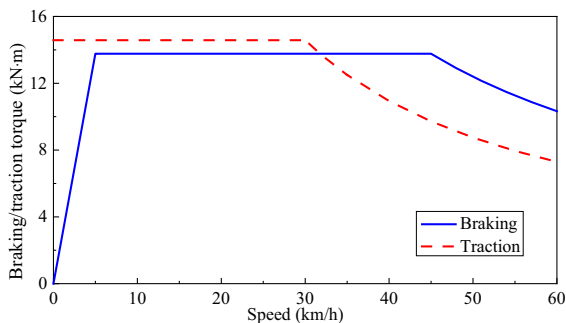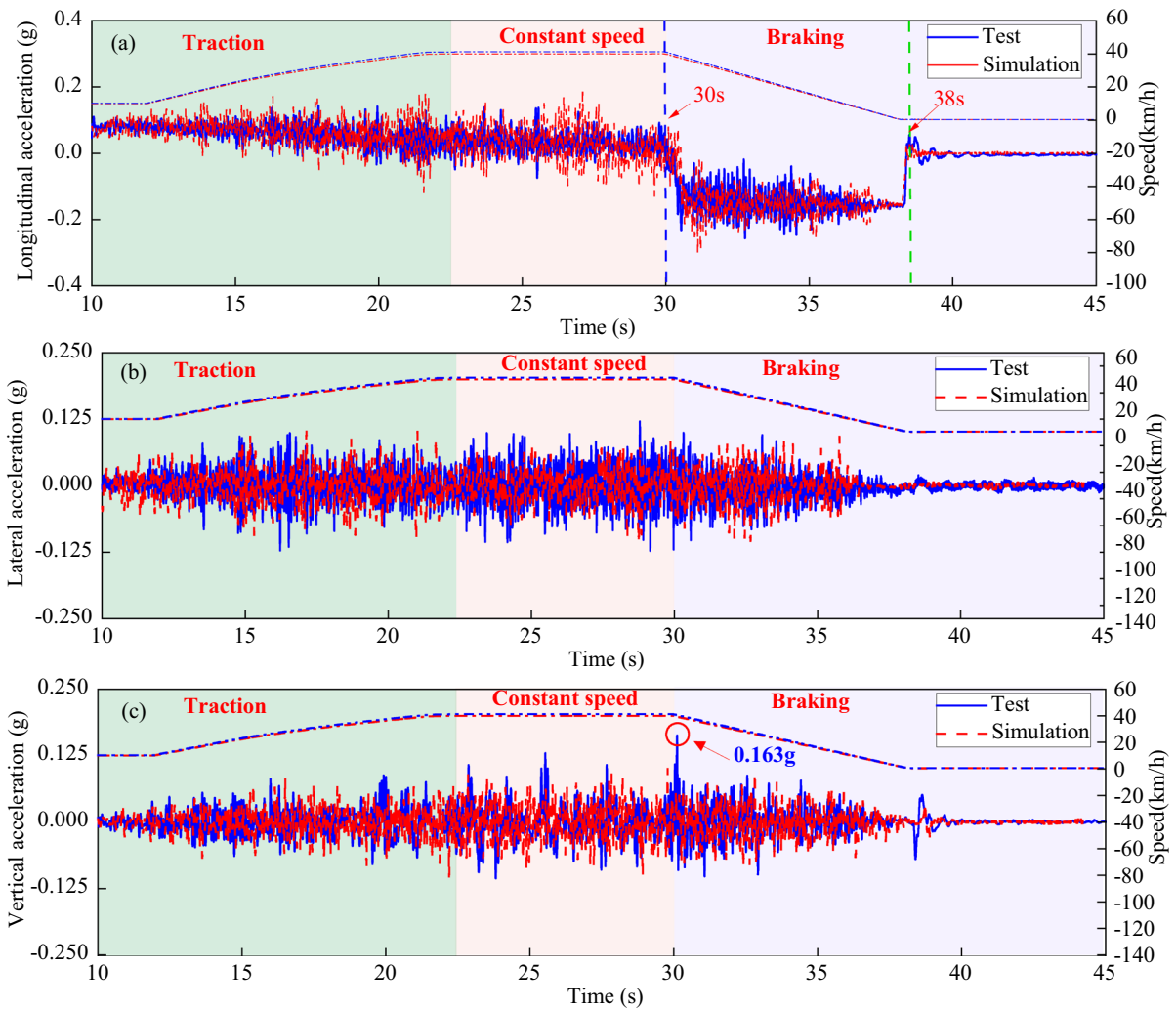
Fig. 13 Traction and braking characteristic curves of SMV

Table 4 Main parameters of the line

Cross Section of track beam (m)	Span of track beam (m)	Cross section of pier (m)	Height of pier (m)	Total length (m)
0.78 × 1.10	25.00	0.80 × 0.80	10.80	550.00

Fig. 14 Vibration acceleration of the monorail vehicle: **a** Longitudinal; **b** Lateral; **c** Vertical

longitudinal vibration frequency f_{bll} and 1st coupled lateral-and-torsional vibration frequency f_{bl1} observed from the simulation and field test results are also close, as shown in Fig. 18a, b.

The aforementioned analysis results demonstrate that the proposed model can effectively capture the deformation and vibration characteristics of the bridge subsystem under stochastic excitation.

4 Results and discussions

The major purpose of the present section is to investigate the impact of variable speed operations and wheel-track adhesion conditions on the spatial nonlinear contact behavior between the wheel and track, as well as the 3D coupling vibration characteristics of the SMTBS.

4.1 Effects of variable train speed on vehicle–bridge dynamic responses

To better understand the influences of variable speed operations on the dynamics performances of SMTBS, the vehicle–bridge dynamic responses obtained from the proposed model under the constant speed and braking conditions are compared.
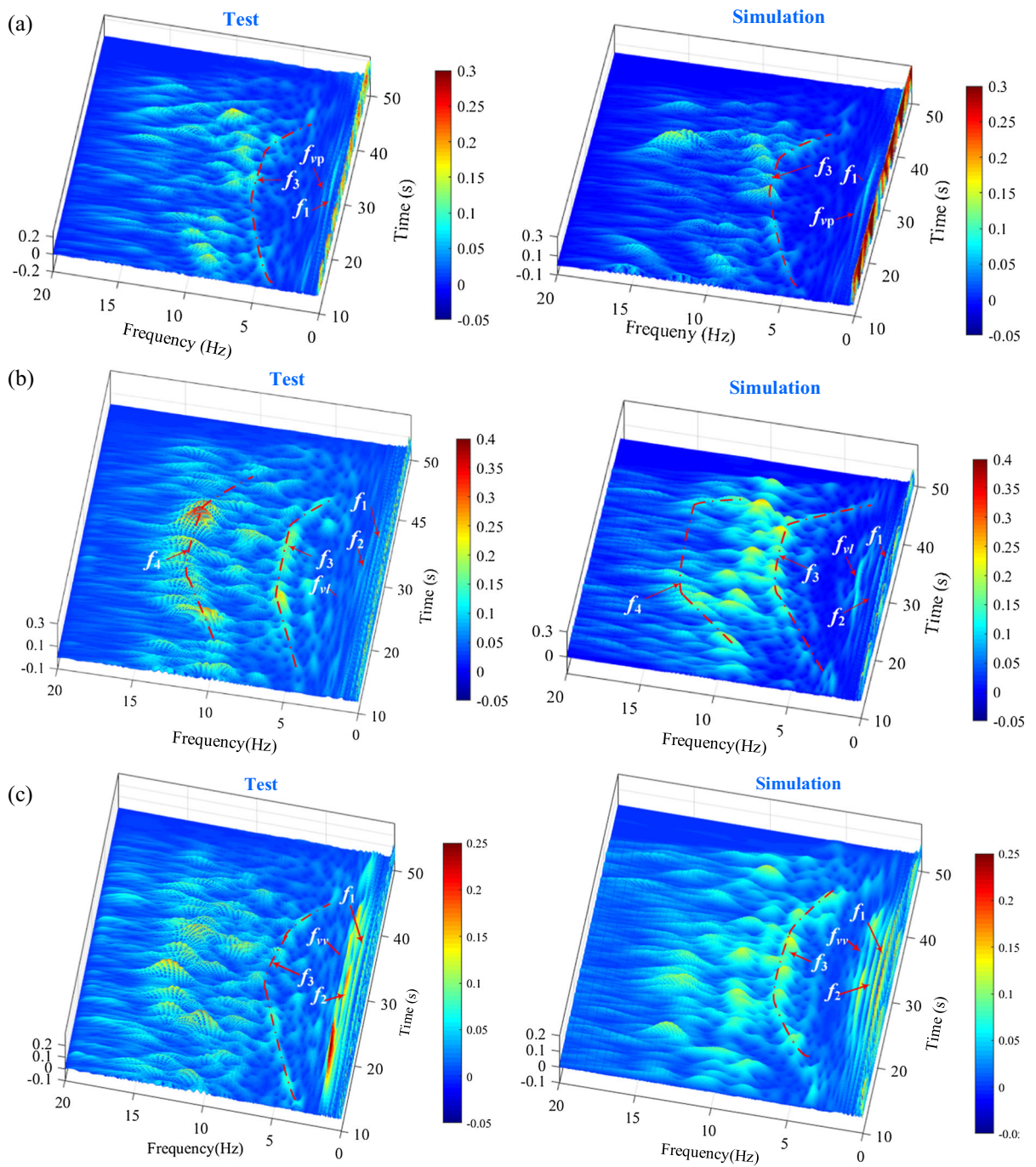
Fig. 15 Vibration acceleration of the SMV in the frequency domain: **a** Longitudinal; **b** Lateral; **c** Vertical
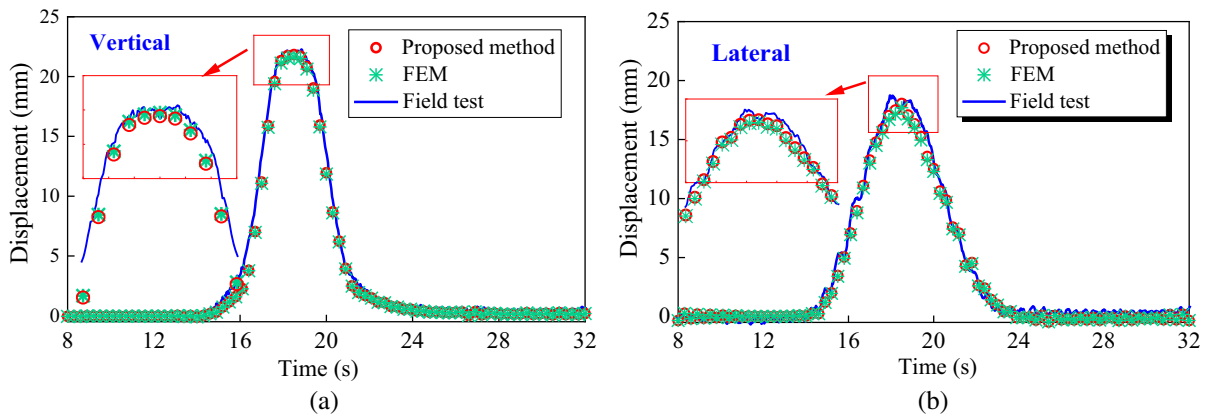
Fig. 16 Comparison of bridge displacement between simulation and field test: **a** Vertical; **b** Lateral
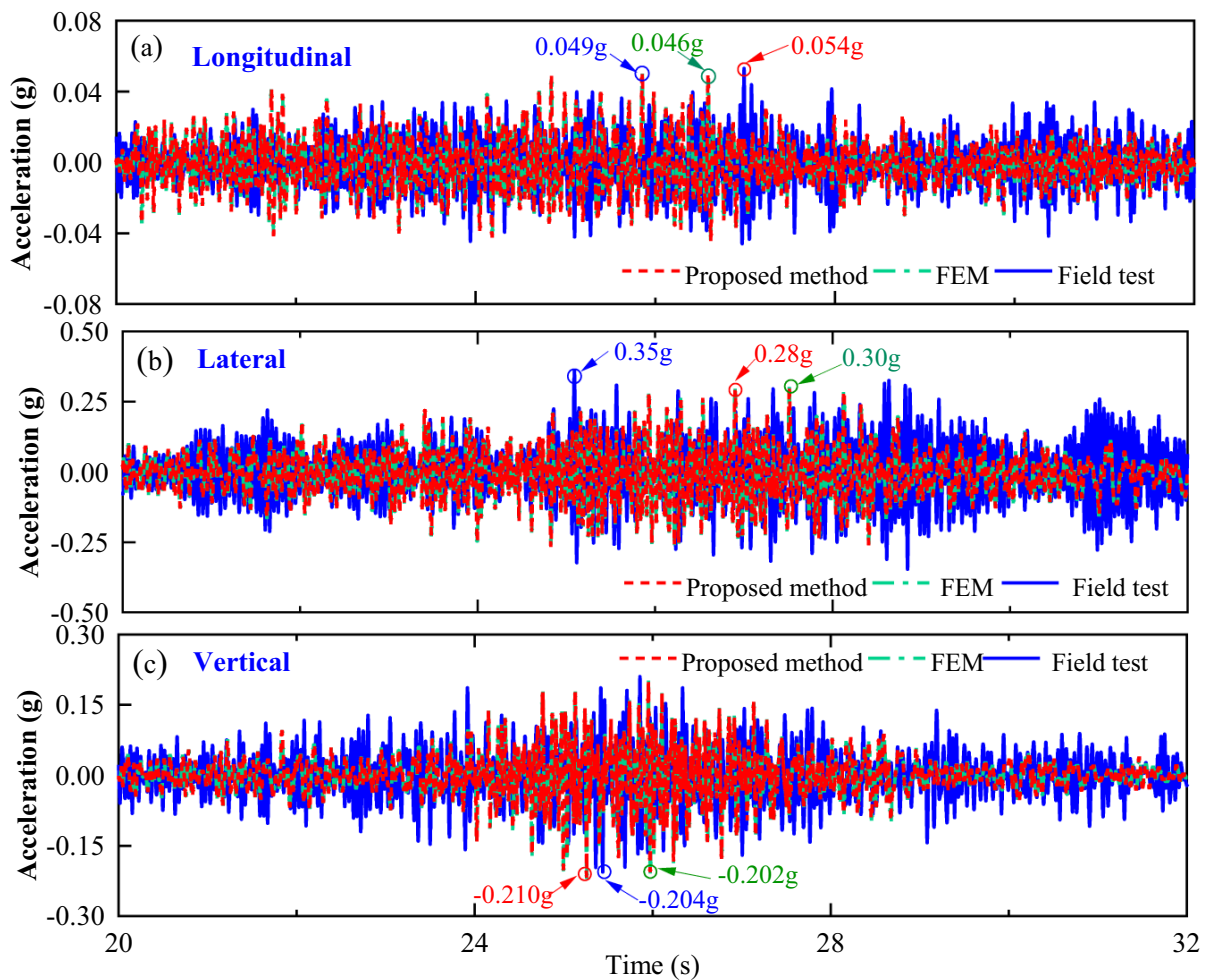

Fig. 17 Comparison of bridge acceleration between simulation and field test: **a** Longitudinal; **b** Lateral; **c** Vertical

Table 5 Computational time comparison between the proposed method and FEM

Method	Modal analysis		Dynamic simulation	
	DOFs	Computational time	DOFs	Computational time
Proposed method	200	12.5 s	200	56 min
FEM	377,970	1500 s	377,970	308 min

4.1.1 Comparison between constant and variable speeds

In this case, a train with three vehicles travels through the track beam under the excitation of track irregularities using a constant friction coefficient of 0.60 [8]. The constant speed condition is 40 km/h and the braking process decelerates from 40 to 5 km/h. The wheel-track dynamic responses involving vertical forces, longitudinal forces, and creepages on different axles are obtained first, as shown in Fig. 19.

Compared with constant speed, the vertical force on axle 1 decreases and the vertical force on axle 3 increases during the braking process, as illustrated in Fig. 19a. The maximum difference values of the vertical force between two axles are 5.75 kN, which indicates that a significant redistribution of vertical load occurs when the vehicle is subjected to braking. However, the amplitudes of vertical force only increase below 0.3 Hz during the braking process. Besides, it can be observed that the longitudinal force increases dramatically under the braking process and the amplitudes are mainly presented in the frequency range of 7–40 Hz. Despite that the longitudinal forces on both axles are extremely close (in Fig. 19c), axle 1 exhibits a greater longitudinal creepage than axle 3 (in Fig. 19e). This means that the driving tyre on axle 1 generates a greater slipping velocity to produce sufficient longitudinal force, owing to the distinct relationship of the creep force-creepage curve under varying vertical loads, as depicted in Fig. 19f. The analysis results indicate that wheel-track stick–slip behaviors of each diving tyre will present different characteristics stemming from the asymmetric vertical load on each axle during the variable speed process.

In conclusion, the variable speed operations result in a significant redistribution of vertical load and an increase in longitudinal force. To further reveal the corresponding effects on the bridge dynamic responses, Fig. 20 presents the mid-span displacements of the track beam under constant speed and braking conditions.

Due to the sudden change of wheel-track longitudinal force when the braking torques are exerted, the longitudinal displacement of the track beam will generate an oscillatory with a maximum value of 2.14 times as large as that of constant speed, as shown in Fig. 20a. Despite the significant redistribution of vertical load under variable speed operation, the maximum lateral and vertical displacements have only slight differences, which may be mainly attributed to the spacing and way in which wheel-track forces are applied on the bridge. Although the vertical force on axle 3 is growing, it is decreasing on axle 1. Hence, the variation in resultant force is significantly lower than that of an individual wheel.

The vehicle–bridge system presents different coupling features induced by different operation conditions. Hence, the time histories and frequency spectrums of vehicle–bridge vibration accelerations under a low running speed (20 km/h), high running speed (60 km/h), and deceleration from 60 to 20 km/h are obtained from the proposed model, as illustrated in Figs. 21 and 22.

The results depicted in Fig. 21a demonstrate that variable speed operation leads to a rapid increase in the peak value of the longitudinal acceleration of the car body, as compared to those obtained from constant speed conditions. However, the peak values of lateral and vertical accelerations at the braking process fall within the range between those observed at constant speeds of 20 and 60 km/h. Regarding the frequency domain, some characteristic frequencies of the dynamics system can be identified at constant speeds. For instance, the frequencies 0.23, 0.66, 3.46, and 10.4 Hz are characteristic frequencies induced by the span of the track beam ($L_B = 25$ m) and wheelbase of the vehicle ($L_t = 1.6$ m) at constant speeds of 20 and 60 km/h, respectively. Besides, the pitching (f_{vp}), lateral (f_{vl}), and vertical (f_{vv}) frequencies of the car body can also be observed. It is worth noting that the
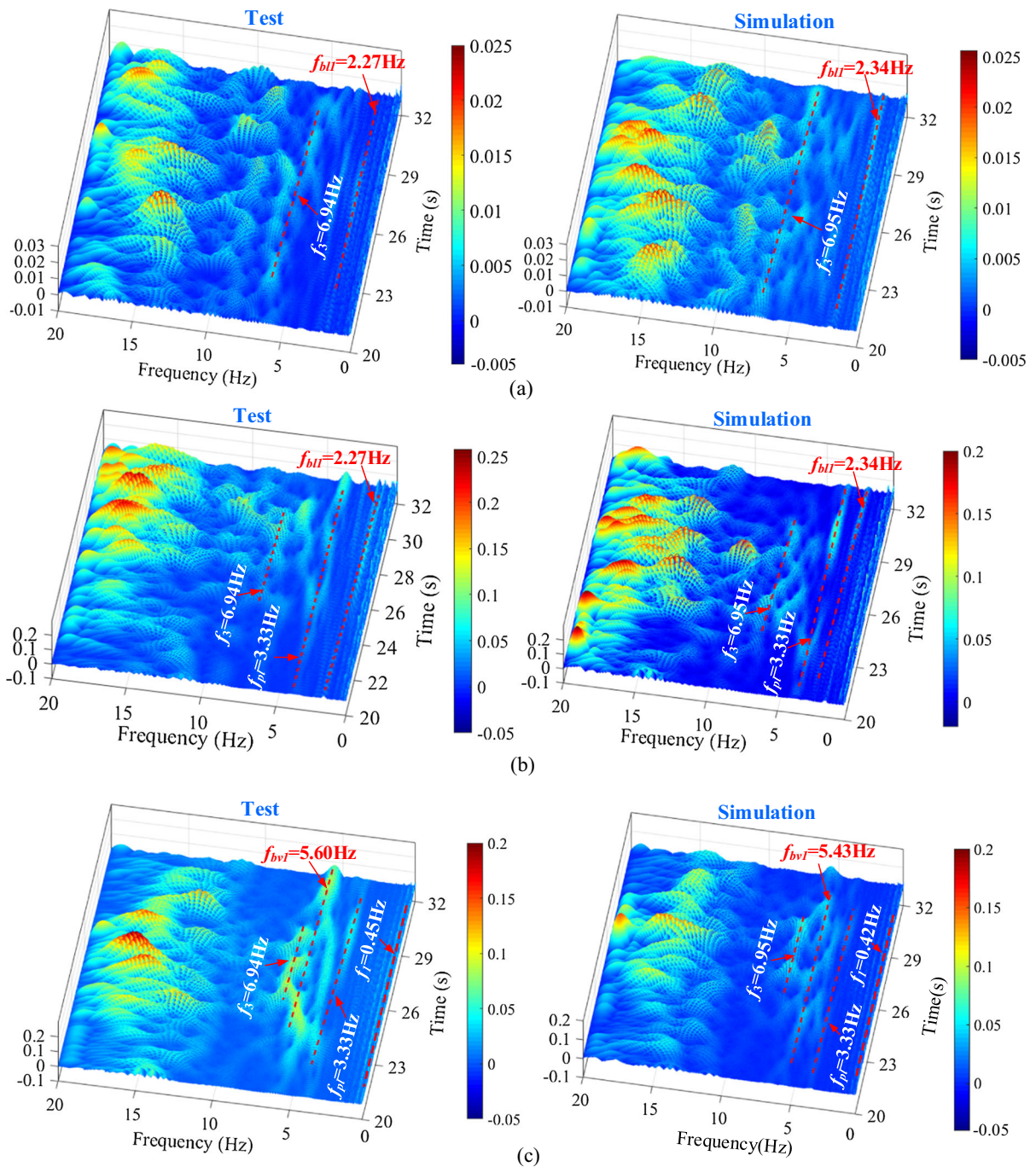
Fig. 18 Spectra comparison of bridge responses between the simulation model and field test: **a** Longitudinal; **b** Lateral; **c** Vertical

peak of f_{vp} induced by variable speed operation is much higher than that under constant speeds of 60 km/h. In particular, the longitudinal acceleration at the range of 2–10 Hz and vertical acceleration at the range of 3–10 Hz are even larger than those at the speed of

60 km/h, indicating that the variable speed operation will intense the longitudinal and vertical vehicle–bridge dynamic interactions at a low-frequency range.

In terms of time-history responses of the bridge accelerations, it can be seen that the longitudinal
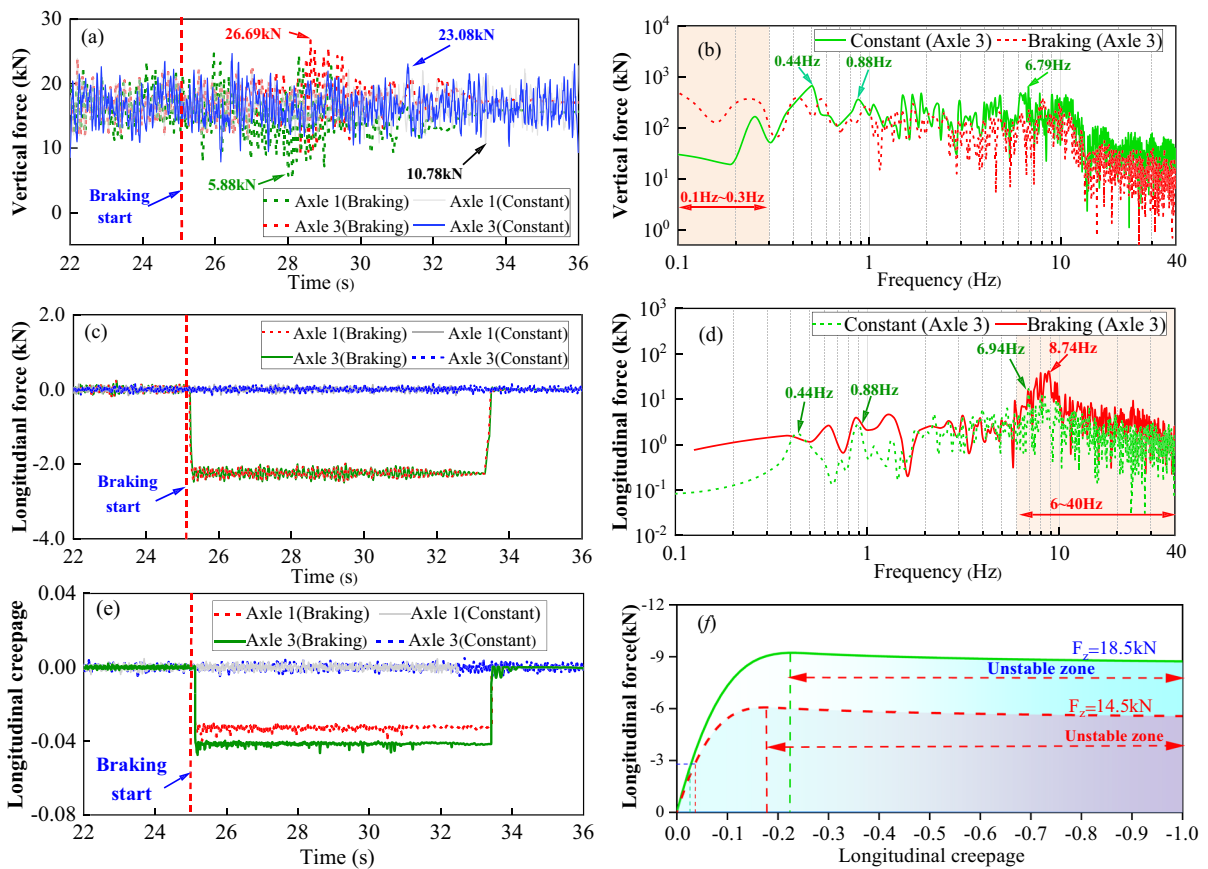
Fig. 19 Dynamic wheel-track forces under constant and variable speed: **a** Vertical forces in time history; **b** Vertical forces in frequency domain; **c** Longitudinal forces in time history; **d** Longitudinal forces in frequency domain; **e** Longitudinal creepages; **f** Creep force-creepage curve under different vertical loads

acceleration of the track beam would significantly increase when the train was subjected to braking compared to the constant speeds. Regarding the frequency domain, some characteristic frequencies of the dynamics system can also be identified at constant speeds. Besides, the longitudinal vibration frequency of the bridge (f_{bll}), lateral bending frequency of the pier ($f_{\mathrm{p}l}$), and the first vertical bending vibration frequency (f_{bv}) of the bridge can also be observed. The peak of f_{bll} in the longitudinal vibration induced by variable speed operation even exceeds that of 60 km/h, while the peaks of other frequencies induced by variable speed fall within the range between those observed at low and high running speeds. It is worth noting that the longitudinal accelerations at the range of 0.7–3 Hz induced by variable speed operation are much larger than those of the speed of 60 km/h, indicating that the variable

speed operation will intensify the longitudinal vehicle–bridge dynamic interactions at a low-frequency range.

The above results show that the longitudinal vibration of the vehicle and bridge increases significantly in the lower frequency range due to the variable speed operation, while only local vertical and lateral vibrations of the vehicle and bridge are amplified.

4.1.2 Effects of initial braking speed

The initial braking speed has important influences on the vehicle–bridge dynamics performances, especially for the longitudinal vibration. To reveal its effects, the longitudinal dynamic responses under different initial braking speeds are investigated, as depicted in Fig. 23.

Figure 23 illustrates the longitudinal dynamic responses of the car body and track beam under
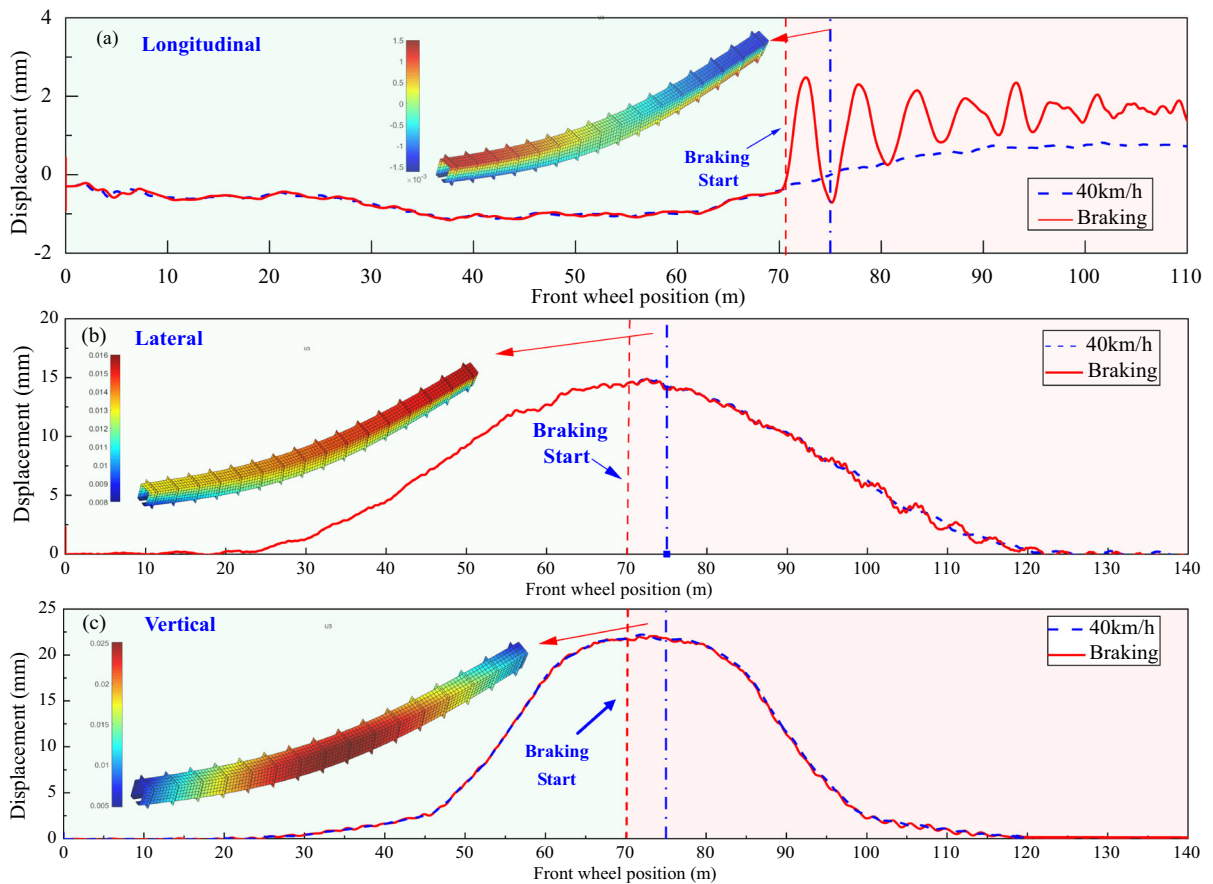
Fig. 20 Displacement of the track beam (Green zone: constant speed; Pink zone: braking): **a** Longitudinal; **b** Lateral; **c** Vertical

different braking speeds. One can observe that the peaks of both the car body and track beam acceleration exhibit a significant increase as braking speeds rise. Analogous conclusions can be drawn from the spectral responses. It is worth noting that the peaks of car-body pitching frequency f_{vp}, the longitudinal vibration frequency of the bridge f_{bll}, lateral bending frequency of the pier f_{pl} all increase with the rising braking speeds. Further, it can be seen from Fig. 23e that an increase in the initial braking speed would also intensify the pitching motion of the car body, which will cause more notable axle load transformation and thus change the state of the wheel-track longitudinal slipping behaviours. In terms of the track beam, an increase in the initial braking speed would result in a larger oscillation of the longitudinal displacement, as portrayed in Fig. 23f. The maximum oscillation amplitude of the longitudinal displacement even reaches 3.72 mm at the initial braking speed of

60 km/h. It is revealed that the longitudinal stability of the bridge would be aggravated due to the increasing initial braking speeds.

4.2 Evaluation of wheel-track interfacial friction performance

4.2.1 Effects of interfacial friction coefficient

The wheel-track interfacial friction coefficient highly depends on the wheel-track interfacial contact status, such as the interfacial materials and environment. Noteworthily, the driving track with welded steel may be moist in winter or the early morning in summer, which could cause inadequate wheel-track interfacial friction force and the slip of the driving tyre, and thus deteriorating vehicle dynamics performances.

To investigate the effects of the wheel-track interfacial friction coefficient, dynamic responses of
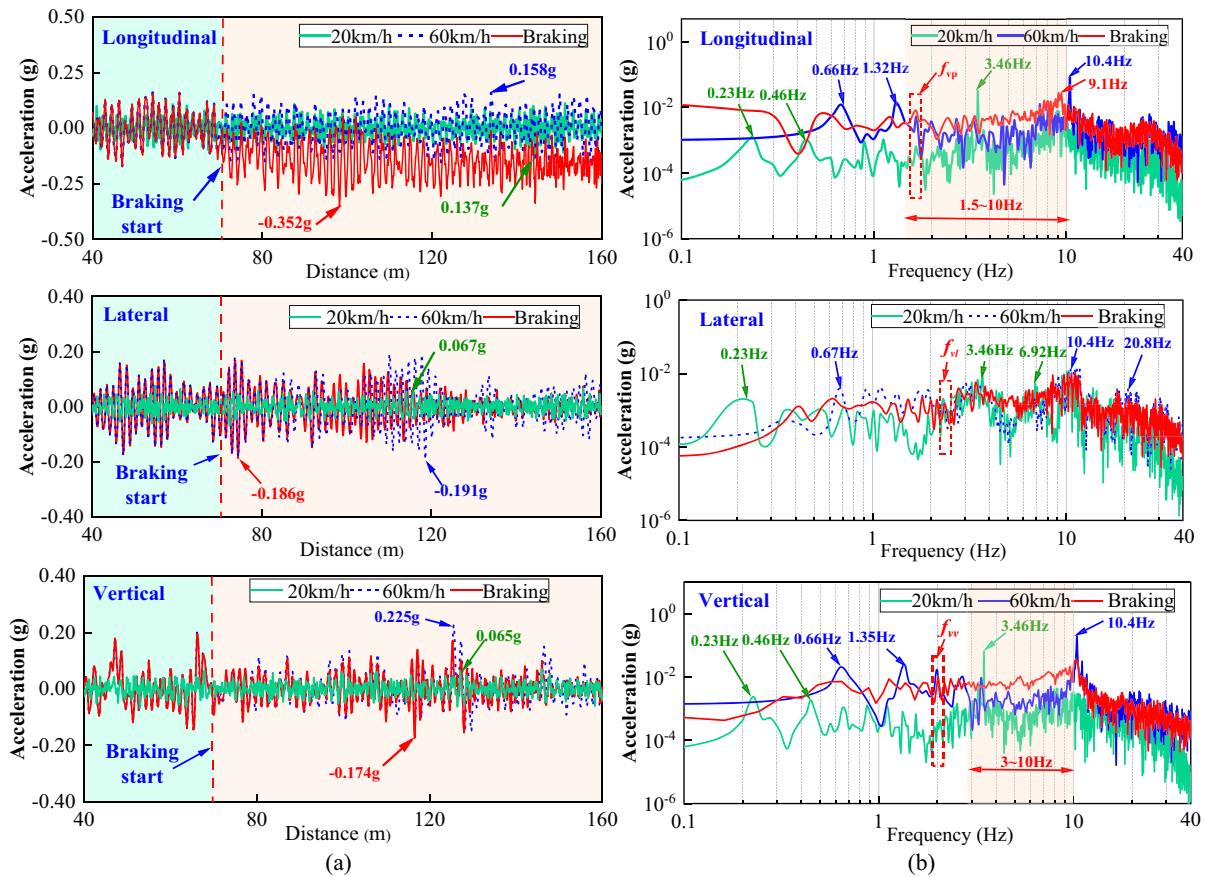
Fig. 21 Vibration acceleration of the car body in time history and frequency domain (Green zone: constant speed; Pink zone: braking): **a** Longitudinal; **b** Lateral; **c** Vertical

SMTBS under different contact conditions are derived from the proposed model, as shown in Figs. 24, 25 and 26. In the simulation, the train is decelerating from 40 to 5 km/h. Specifically, a friction coefficient of 0.6 represents dry adhesion condition while a value of 0.15 indicates wet adhesion condition.

As illustrated in Fig. 24a, under the train braking condition, the vertical tyre force under the friction coefficient of 0.60 is slightly larger than that under the friction coefficient of 0.15, showing that the friction coefficient has small influences on the redistribution of vertical axle load. Similar results can be seen in the frequency domain. However, significant oscillation can be observed in the longitudinal force under a lower friction coefficient with a maximum amplitude of 1.3 kN. The increases in amplitudes are mainly present in all observed frequency bands, as shown in Fig. 24d. Besides, the longitudinal creepage would

also significantly increase, which implies that too small wheel-track friction coefficients may cause tyre slip when the train is subject to brake. The phenomenon is attributed to the distinct relationship of the creep force-creepage curve under different friction coefficients, and an unstable state arises when longitudinal forces shift from the linear to nonlinear region, particularly at low friction coefficients, as shown in Fig. 24f. In some special operating conditions, this may pose a threat to the safety of vehicle operation, especially for the emergency braking of the train running on a long slope line under urgent conditions.

Furthermore, the vibration acceleration of the car body and track beam are also extracted, respectively, as shown in Figs. 25 and 26. The braking process is highlighted in the green and pink zones.

In the time history, one can observe that a smaller friction coefficient would cause increases in the
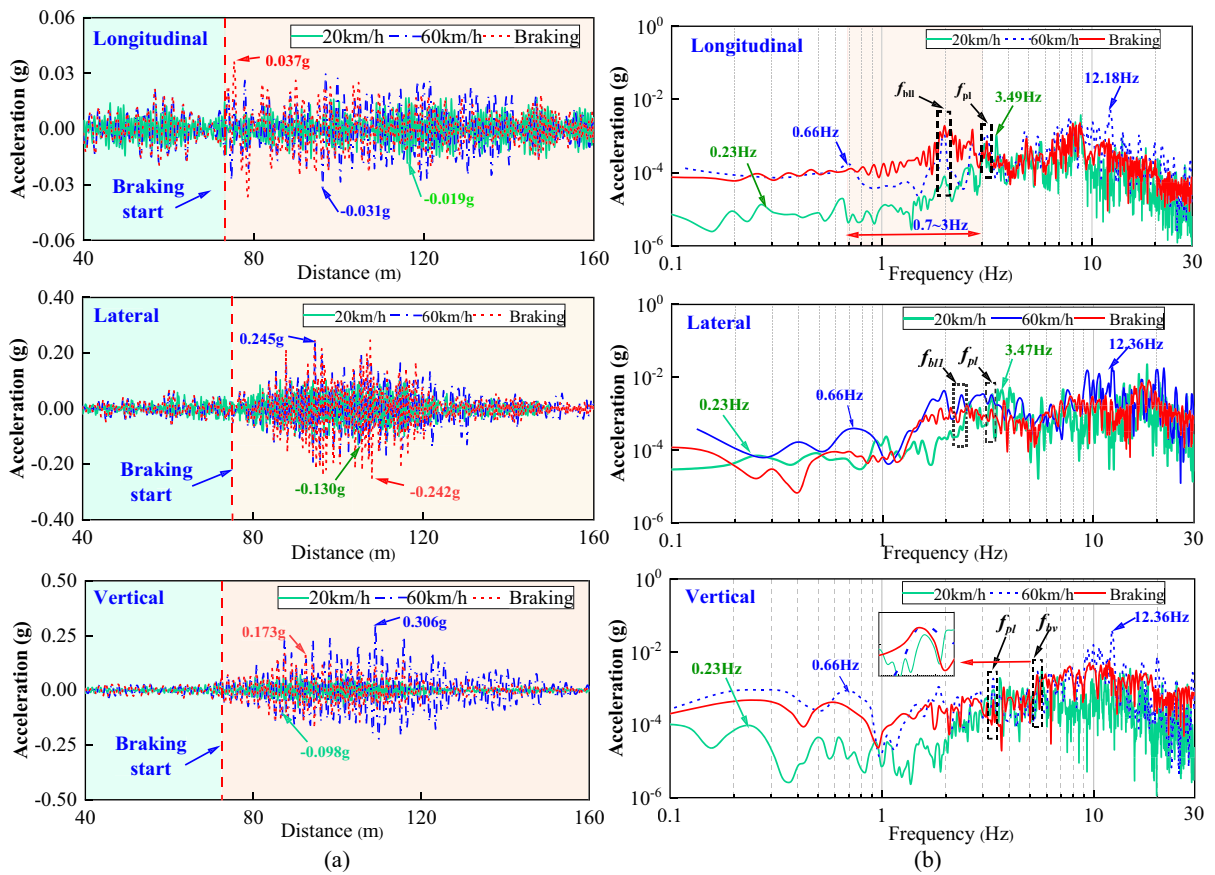
Fig. 22 Vibration acceleration of the track beam in time history and frequency domain (Green zone: constant speed; Pink zone: braking): **a** Time history; **b** Frequency domain

longitudinal, lateral, and vertical accelerations of the vehicle. Especially, the longitudinal acceleration of the car body under the friction coefficient of 0.15 is 1.14 times as large as that under a friction coefficient of 0.60. In the frequency domain, the increases of the amplitude mainly are observed between 25–30 Hz and below 2 Hz. It is worth noting that the amplitudes of the load frequencies 0.45, 0.90, and 6.89 Hz also increase under the inadequate friction coefficient. This can be attributed to the fact that the longitudinal force of the tyre appears a significant oscillation under wet adhesion conditions (in Fig. 25c, d). Regarding the vertical vibration, the acceleration of the car body is 1.08 times greater when the friction coefficient is 0.15 compared to that when it is 0.60, and the frequency differences are mainly presented in the ranges of 2–7 Hz and 10–40 Hz. However, slight discrepancies can be seen in the lateral vibration of the car body, which is mainly concentrated below 10 Hz. The

analysis results indicate that the inadequate friction coefficient will result in significant longitudinal and vertical vibrations of the car body.

In terms of the track beam vibration, the analogous phenomenon can be found in Fig. 26. It can be observed that the maximum values of longitudinal, lateral, and vertical accelerations of the track beam under the friction coefficient of 0.15 are respectively about 1.8, 1.35 and 1.59 times as large as those under the friction coefficient of 0.60. As for the frequency domain, the increase in longitudinal vibration is below 4.13 Hz, whereas the lateral and vertical vibrations exhibit an increase in higher frequency ranges, specifically between 7–20 and 4–14 Hz, respectively. Additionally, an inadequate friction coefficient will result in significant longitudinal vibration (f_{bll}) and first bending vibration (f_{bv1}). The research results show that adhesion conditions have a significant effect on the VBI of the SMTBS, highlighting the importance of
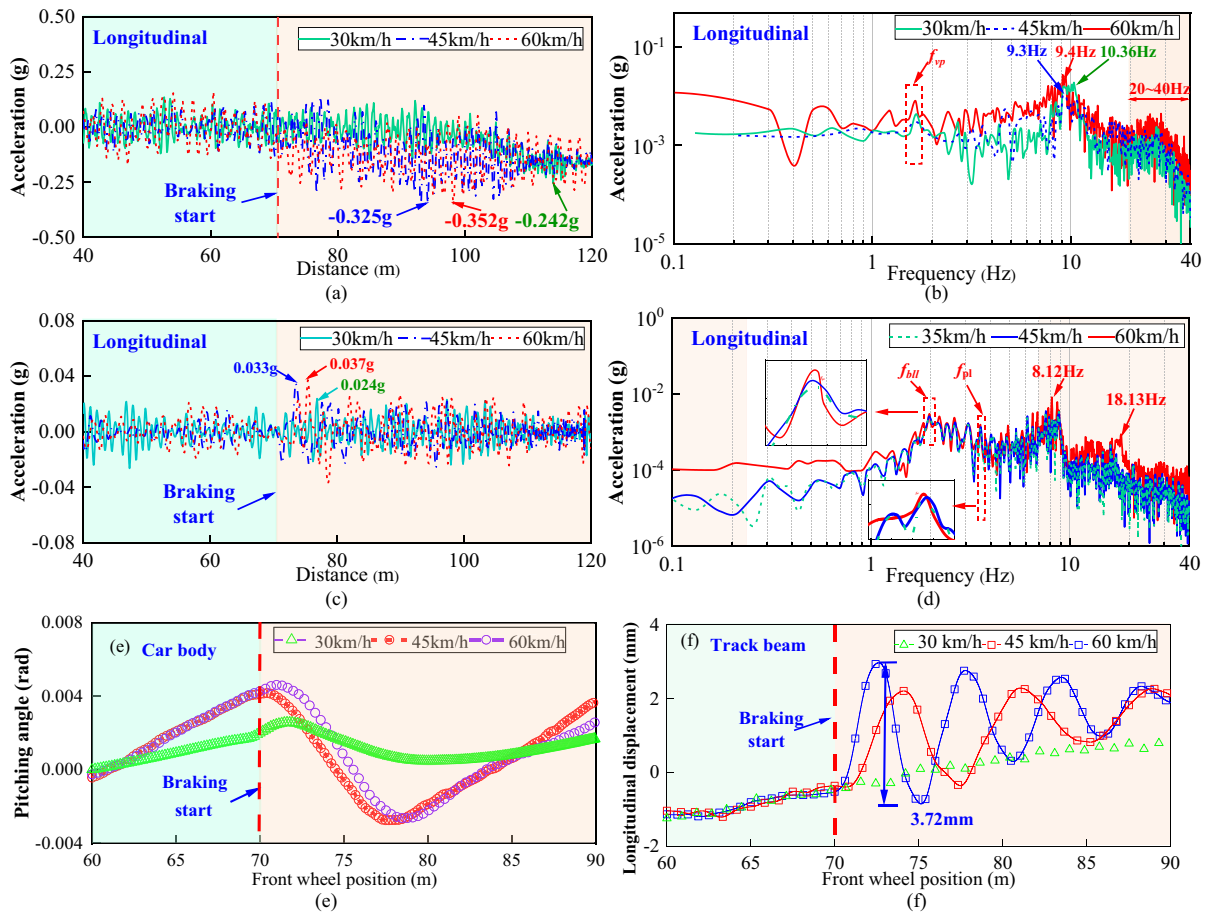
Fig. 23 Longitudinal responses of SMTBS under different initial braking speeds: **a** Time history of car body acceleration; **b** Frequency spectrum of car body acceleration; **c** Time history of the track beam acceleration; **d** Frequency spectrum of the track beam acceleration; **e** Pitching angle of car body; **f** Longitudinal displacement of the track beam

considering wheel-track slipping behavious when investigating spatial coupling characteristics of SMTBS under variable speed conditions.

4.2.2 Limit value of interfacial friction coefficient

As presented above, a low friction coefficient may pose a threat to the running safety of the vehicle. Hence, it is imperative to determine an appropriate interfacial friction coefficient between the wheel and track. Considering that normal load distribution will affect wheel-track slipping behavior, the longitudinal responses of monorail vehicles are obtained under different amplitudes of track irregularity (TI), as illustrated in Fig. 27. The track excitations are referred to as road irregularity [61] and the corresponding wavelength range is 0.1–25 m.

As depicted in Fig. 27, the longitudinal creepage exhibits a sharp increase when the interfacial friction coefficient falls below 0.35 (in Fig. 27a), resulting in more pronounced oscillations of longitudinal forces (in Fig. 27b). Furthermore, the oscillation amplitude of longitudinal force rises with increasing track irregularity amplitude, thereby forming nonlinear friction boundaries, as indicated by the red line in Fig. 27b. It can be also observed that the presence of severe track irregularities can result in violent oscillations of the vertical force and thus leading to significant changes in longitudinal forces within this region (in Fig. 27b). When the friction coefficient is less than 0.35, an increase in the amplitude of track irregularity results in a decrease in the boundary of the friction coefficient. Taking 0.25 g as the limit value of car body longitudinal acceleration, a nonlinear friction
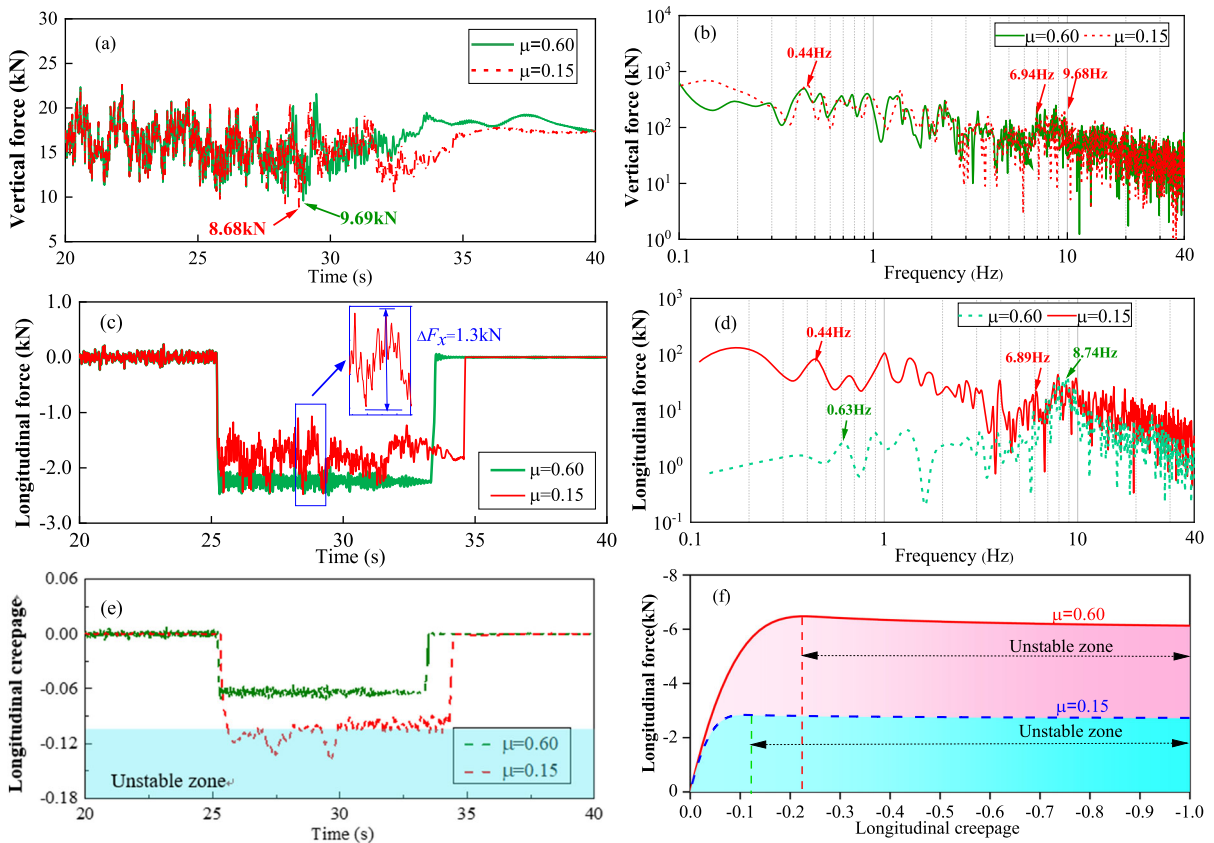
Fig. 24 Wheel-track forces of SMTBS under different interfacial friction coefficients: **a** Vertical force in time domain; **b** Vertical force in frequency domain; **c** Longitudinal force in time domain; **d** Longitudinal force in the frequency domain; **e** Longitudinal creepage; **f** Creep force-creepage curve under different friction coefficient

boundary will form, as shown by the red line in Fig. 27c. The main reason is that the longitudinal vibration of the vehicle is susceptible to the effect of wheel-track slipping under lower adhesion.

As mentioned above, vertical loads of the driving tyre have a significant effect on wheel-track stick–slip behavior. The worse the track irregularity is, the more significant the influence is on the wheel-track longitudinal vibration. Hence, the limit value of the friction coefficient should be determined based on the amplitude of track irregularity. For instance, when the amplitude is 6 mm, it is recommended to maintain an interfacial friction coefficient greater than 0.35 during wet weather conditions to mitigate the longitudinal impact on monorail vehicles during the braking process.

5 Conclusion and future works

This work presents an effective 3D train–bridge interaction model for monorail systems considering nonlinear wheel-track slipping behavior, aiming to investigate the spatial wheel-track nonlinear contact behavior and 3D coupling vibration of the SMTBS. By comparison of simulation results and test data under different operating conditions, the reliability of the proposed model has been validated. On this basis, the nonlinear wheel-track slipping behaviors and their influences on the dynamics performances of SMTBS are researched under variable speed operation. The reasonable wheel-track interfacial friction coefficient is also recommended to ensure good vehicle dynamics performances. The main conclusions can be drawn as follows:

(1) Dynamic responses obtained by the proposed coupling dynamics model are in good
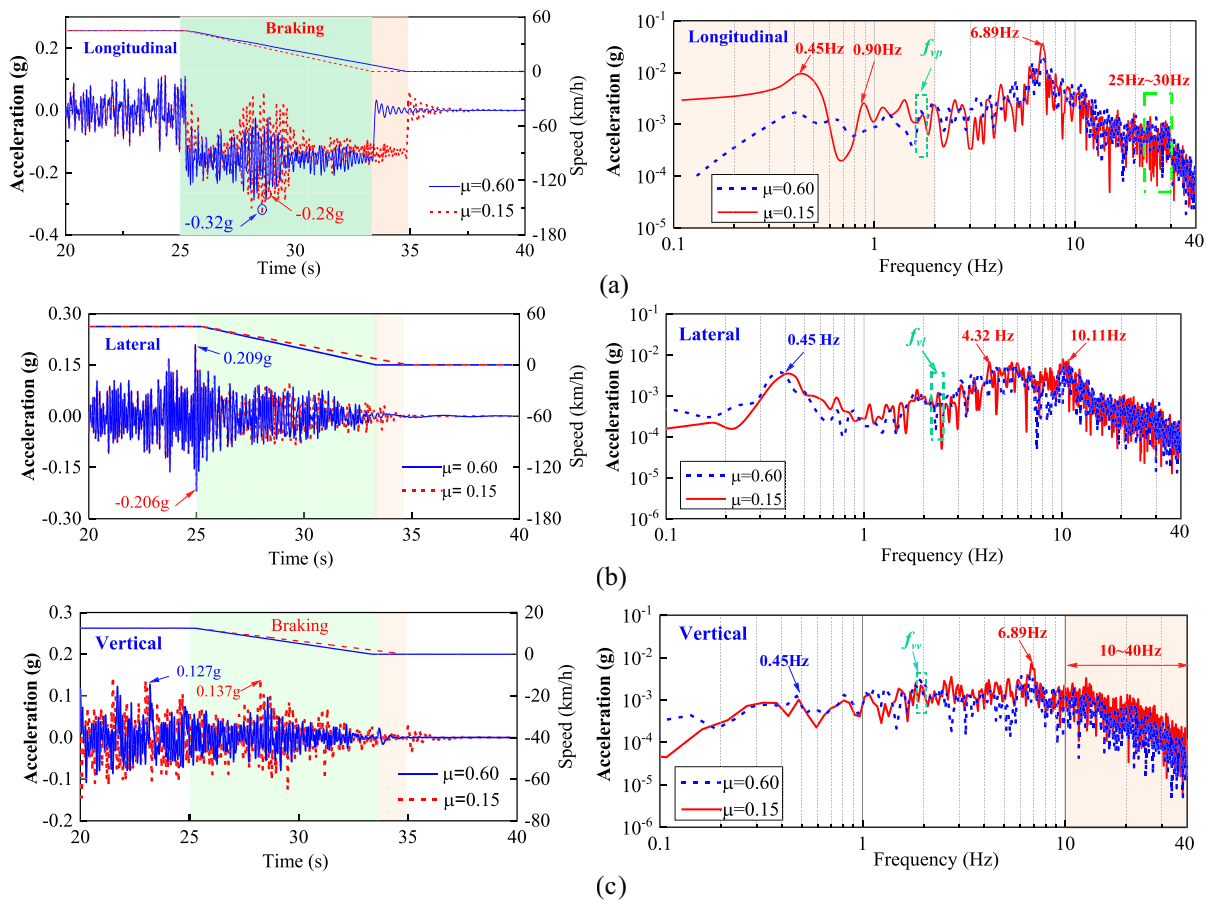
Fig. 25 Vibration acceleration of the car body under different adhesion conditions in time history and the frequency domain: **a** Longitudinal acceleration; **b** Lateral acceleration; **c** Vertical acceleration

agreement with those of the field test data in time and frequency domains, indicating that the proposed model is reliable to be used for investigating the time-varying coupling features of SMTBS under variable speed conditions.

(2) Both the track irregularity and loading moving frequency of SMTBS have significant effects on the DMPF of the bridge. The redefined DMPF could better assess the influence of the track irregularity and loading moving frequency on the convergence of the bridge, which would be more accurate in the evaluation and selection of the modal truncation frequencies of the bridge.

(3) Under braking conditions, both significant redistribution of vertical axle load and longitudinal slip of the driving tyre is likely to occur.
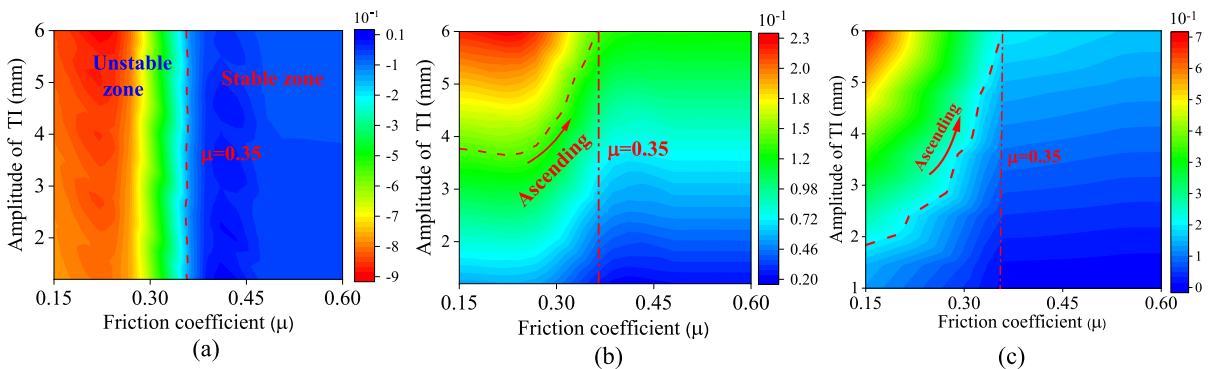
Additionally, the car-body longitudinal acceleration and longitudinal displacements of the tack beam would also generate obvious oscillatory amplitudes. With an increase in the initial braking speed, the longitudinal vehicle–bridge dynamic responses would be significantly intensified, especially for the pitching motion of the car body and longitudinal displacements of the tack beam.

(4) The developed spatial wheel-track contact model is capable of simulating the nonlinear slipping behavior of the wheel-track system under varying friction coefficients and different vertical loads. Besides, the longitudinal stick–slip behavior is significantly affected by the vertical axle load on the driving tire. As track
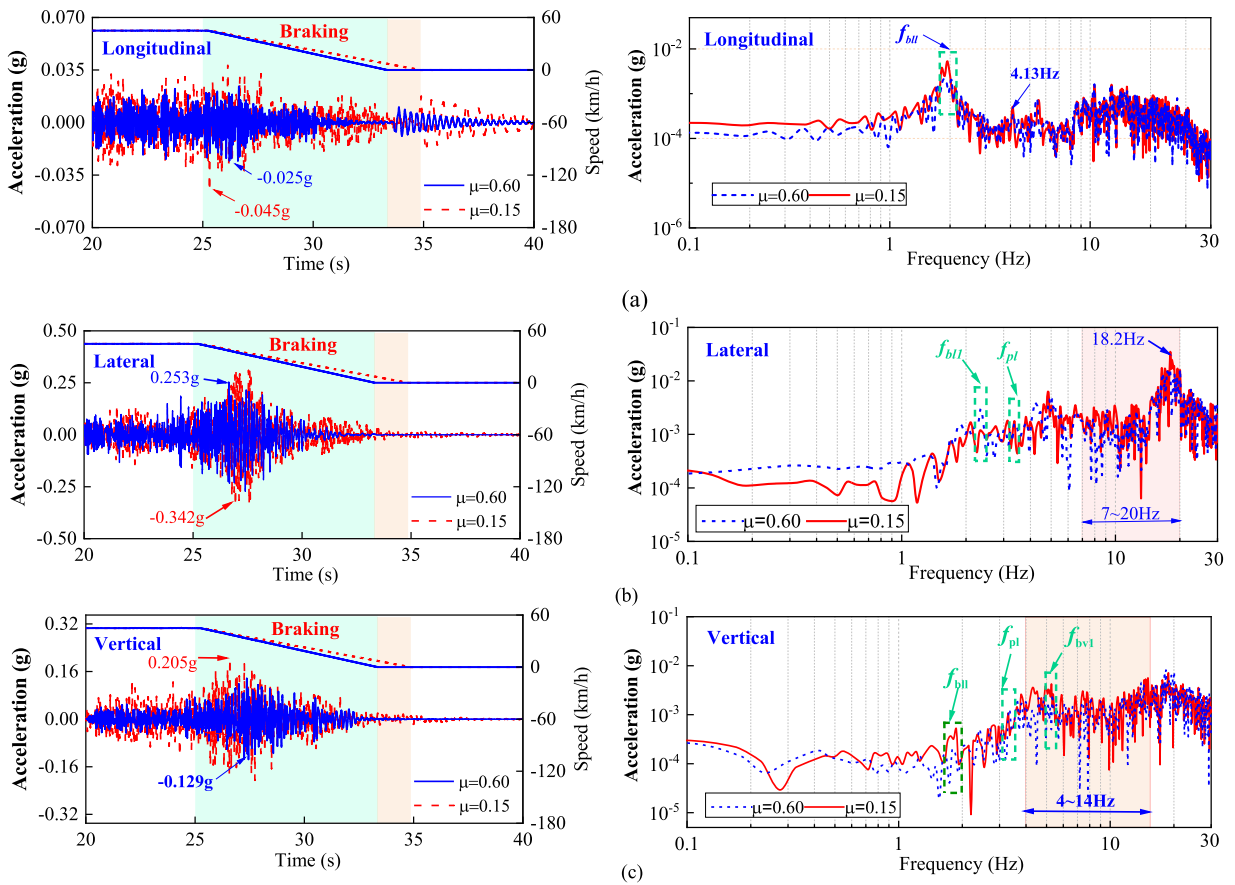
Fig. 26 Vibration acceleration of the track beam under different adhesion conditions in time history and the frequency domain: **a** Longitudinal acceleration; **b** Lateral acceleration; **c** Vertical acceleration

Fig. 27 Longitudinal dynamic responses under different adhesion conditions and different amplitudes of track irregularity: **a** Longitudinal creepage; **b** Longitudinal force; **c** Longitudinal acceleration of the car body

irregularities worsen, this influence becomes increasingly pronounced in terms of wheel-track longitudinal vibration. To ensure a good vehicle–bridge dynamics performance, it is suggested that the interfacial friction coefficient should be larger than 0.35.

The proposed 3D train–bridge interaction model for monorail systems adequately considers the influence of the nonlinear wheel-track slipping behavior, and it is comprehensively validated by the field test. The proposed model could be further applied to evaluate the spatial wheel-track contact behavior, vehicle running safety, and bridge dynamic performance of the SMTBS under complex line conditions in the future, such as the curved lines with a small radius and the lines with a steep slope, which could provide a useful guide for the optimization design and operation safety of the SMTBS.

Authors' contributions Yun Yang: Methodology, Software, Validation, Writing—original draft. Qinglie He: Conceptualization, Funding acquisition, Writing—review & editing, Supervision. Chengbiao Cai: Conceptualization, Funding acquisition, Writing—review & editing, Supervision. Shengyang Zhu: Writing—review & editing, Supervision. Wanming Zhai: Writing—review & editing, Supervision.

Data availability The data that support the findings of this study are available from the corresponding author upon reasonable request.

Declarations

Conflict of interest The authors declare that they have no known competing financial interests or personal relationships that could have appeared to influence the work reported in this paper.

$$\mathbf{F}_{c\mathrm{int}} = \begin{bmatrix} \mathbf{F}_{cx\mathrm{int}} \\ \mathbf{F}_{cy\mathrm{int}} \\ \mathbf{F}_{cz\mathrm{int}} \\ \mathbf{F}_{c\theta\mathrm{int}} \\ \mathbf{F}_{c\beta\mathrm{int}} \\ \mathbf{F}_{c\varphi\mathrm{int}} \end{bmatrix}$$

$$= \begin{bmatrix} F_{dxLi} + F_{dxRi} + F_{copf} - F_{copr} \\ \sum_{k=1}^{2} \left(F_{dyLi}\cos\theta_{li} - F_{dyRi}\cos\theta_{ri} \right) + F_{shfi} + F_{shbi} + F_{rbLi} + F_{rbRi} \\ -\sum_{k=1}^{2} \left(F_{dzLi}\sin\theta_{li} + F_{dzRi}\sin\theta_{ri} \right) \\ \sum_{k=1}^{2} \left(F_{dzLi}\sin\theta_{li} - F_{dzRi}\sin\theta_{ri} \right)h_1 + \sum_{k=1}^{2} \left(F_{dzLi}\cos\theta_{li} - F_{dzRi}\cos\theta_{ri} \right)h_1 + \sum_{k=1}^{2} F_{shi}h_{h3} + \sum_{k=1}^{2} F_{rbli}h_h \\ \sum_{k=1}^{2} (-1)^{k+1} \left(F_{dzfLi}\sin\theta_{fli} + F_{dzfRi}\sin\theta_{fri} \right)s_1 \\ \sum_{k=1}^{2} (-1)^{k+1} \left(F_{dzfLi}\cos\theta_{fli} - F_{dzfRi}\cos\theta_{fri} \right)s_1 + \sum_{k=1}^{2} (-1)^{k+1} F_{shi}s_2 + \sum_{k=1}^{2} F_{rLi}h \end{bmatrix}$$

(A.3)

$$\mathbf{F}_{c\mathrm{int}} = \begin{bmatrix} \mathbf{F}_{tkx\mathrm{int}} \\ \mathbf{F}_{tky\mathrm{int}} \\ \mathbf{F}_{tkz\mathrm{int}} \\ \mathbf{F}_{tk\theta\mathrm{int}} \\ \mathbf{F}_{tk\beta\mathrm{int}} \\ \mathbf{F}_{tk\varphi\mathrm{int}} \end{bmatrix}$$

$$= \begin{bmatrix} F_{sxLi} + F_{sxRi} + \sum_{k=1}^{2}\sum_{i=1}^{2}\left(F_{dtxLki} + F_{dtxRki}\right) \\ -\left(F_{syLi} + F_{syRi}\right) + \sum_{k=1}^{2}\sum_{i=1}^{2}\left(F_{gtLki} + F_{gtRki}\right) + \sum_{k=1}^{2}\sum_{i=1}^{2}\left(F_{dtyLki} + F_{dtyRki}\right) \\ F_{szLi} + F_{szRi} - \sum_{k=1}^{2}\sum_{i=1}^{2}\left(F_{dtzLki} + F_{dtzRki}\right) + M_{ti}g \\ \left(F_{szRi} - F_{szLi}\right)b_2 + \left(F_{syLi} + F_{syRi}\right)\mathrm{H}_{dt} + \sum_{k=1}^{2}\sum_{i=1}^{2}\left(-1\right)^{i+1}\left(F_{dtzfLki} - F_{dtzfRki}\right)b_4 \\ \left(F_{sxLi} + F_{sxRi}\right)\mathrm{H}_{dt} + \sum_{k=1}^{2}\sum_{i=1}^{2}\left(-1\right)^{i+1}\left(F_{dtzLki} + F_{dtzRki}\right)S_3 + M_{rr} \\ -\left(F_{cpL} - F_{cpR}\right)s_3 + \sum_{k=1}^{2}\sum_{i=1}^{2}\left(-1\right)^{i+1}\left(F_{gtzLki} + F_{gtzRki}\right)s_2 + M_{zL} + M_{zR} \end{bmatrix} \tag{A.4}$$

$$\mathbf{F}_{hk\mathrm{int}} = \begin{bmatrix} \mathbf{F}_{hkx\mathrm{int}} \\ \mathbf{F}_{hky\mathrm{int}} \\ \mathbf{F}_{hkz\mathrm{int}} \\ \mathbf{F}_{hk\theta\mathrm{int}} \\ \mathbf{F}_{hk\beta\mathrm{int}} \\ \mathbf{F}_{hk\varphi\mathrm{int}} \end{bmatrix}$$

$$= \begin{bmatrix} F_{cbi} - \left(F_{sxLi} + F_{sxRi}\right) \\ F_{syLi} + F_{syRi} - F_{ddLi}cosq_{fli} + F_{chRi}cosq_{fri} - F_{s/fi} - F_{rbLi} \\ F_{dzfli}sin\theta_{fli} + F_{dzfri}sin\theta_{fri} - F_{szli} - F_{szri} + M_{sd} \\ \left(F_{szLi} - F_{szRi}\right)b_2 + \left(F_{syLi} + F_{syRi}\right)h_6 + \left(F_{dzLi}cos\theta_{li} - F_{dzRi}cos\theta_{ri}\right)h_7 + \left(F_{dzRi}sin\theta_{ri} - F_{dzLi}sin\theta_{li}\right)h_7 \\ +F_{shfi}h_3 + F_{rbli}h_h - M_{krg} \\ \left(F_{sxLi} + F_{sxRi}\right)H_{dt} + F_{dxfi}h_7 \\ 0 \end{bmatrix} \tag{A.5}$$

Appendix A

The mass matrices and internal force matrices for vehicle subsystem can be written as:

$$\mathbf{M}_v = diag[\mathbf{M}_c\ \mathbf{M}_{t1}\ \mathbf{M}_{t2}\ \mathbf{M}_{h1}\ \mathbf{M}_{h2}\ \mathbf{M}_{w1}\ \mathbf{M}_{w2}\ \mathbf{M}_{w3}\ \mathbf{M}_{w4}]$$

(A.1)

$$
\begin{aligned}
\mathbf{M}_c &= diag[\,m_c\ m_c\ m_c\ J_{cx}\ J_{cy}\ J_{cz}\,], \\
\mathbf{M}_{ti} &= diag[\,m_t\ m_t\ m_t\ J_{tx}\ J_{ty}\ J_{tz}\,] \\
\mathbf{M}_{hi} &= diag[\,m_h\ m_h\ m_h\ J_{hx}\ J_{hy}\ J_{hc}\,], \\
\mathbf{M}_{wi} &= diag[J_{wli}\ J_{wri}]
\end{aligned}
$$

(A.2)

The internal force matrices for car body, bogie, suspended rod, the driving wheel can be written as:

$$
\mathbf{F}_{wk\text{int}} = \begin{bmatrix} \mathbf{F}_{wkx\text{int}} \\ \mathbf{F}_{wky\text{int}} \\ \mathbf{F}_{wkz\text{int}} \\ \mathbf{F}_{wk\theta\text{int}} \\ \mathbf{F}_{wk\beta\text{int}} \\ \mathbf{F}_{wk\varphi\text{int}} \end{bmatrix} = \begin{bmatrix} F_{dtxi} - F_{txi} \\ 0 \\ 0 \\ 0 \\ F_{dtki}R_e - T_{wi} \\ 0 \end{bmatrix}
$$

(A.6)

Secondary suspension forces $\mathbf{F}_{sec}$ are determined by the relative motion relationship between the bolster and the bogie, the matrix form of which can be expressed as:

$$
\mathbf{F}_{sec} = \begin{bmatrix} F_{sx(L,R)i} \\ F_{sy(L,R)i} \\ F_{sz(L,R)i} \end{bmatrix}
$$
$$
= \begin{bmatrix} K_{sx}\left(X_{hi} - X_{ti} - H_{bt}\beta_{hi} - H_{hf}\beta_{ti}\right) + C_{sx}\left(\dot{X}_{hi} - \dot{X}_{ti} - H_{bt}\dot{\beta}_{hi} - H_{hf}\dot{\beta}_{ti}\right) \\ K_{sy}\left(Y_{ti} - Y_{hi} - H_{hf}\phi_{hi} - H_{bt}\phi_{ti}\right) + C_{sy}\left(\dot{Y}_{ti} - \dot{Y}_{hi} - H_{hf}\dot{\phi}_{hi} - H_{bt}\dot{\phi}_{ti}\right) \\ K_{sz}\left(Z_{hi} - Z_{ti} \pm d_s\phi_{ti} \mp d_s\phi_{hi}\right) + C_{sz}\left(Z_{hi} - Z_{ti} \pm d_s\dot{\phi}_{ti} \mp d_s\dot{\phi}_{hi}\right) \end{bmatrix}
$$

(A.7)

where the symbol 'f', 'r', 'L', and 'R' denotes the front, rear, left, and right of the rigid body, respectively; '$\pm$' and '$\mp$' are applied on the left and right sides of each component; $F_{sx(L,R)i}$, $F_{sy(L,R)i}$ and $F_{sz(L,R)i}$ are the longitudinal, lateral and vertical force of secondary suspension, respectively. F_{sh}, F_{rb}, and F_{cop} are the force of the shock absorber, the rubber stop, and the coupler force between the car body. The force of shock absorber can be expressed as:

$$
\begin{aligned}
F_{shi} &= k_{sh}(Y_{hi} - Y_{ci} - b_2\phi_{ci} - b_2\phi_{hi} - s_1\psi_{ci}) \\
&\quad + c_{sh}\left(\dot{Y}_{hi} - \dot{Y}_{ci} - b_2\dot{\phi}_{ci} - b_2\dot{\phi}_{hi} - s_1\dot{\psi}_{ci}\right)
\end{aligned}
$$

(A.8)

$\mathbf{T}_{ui}$ and $\mathbf{T}_{pi}$ are transformation matrices for the upper and lower of the hinge joint, respectively, which can be obtained as:

$$
\begin{aligned}
\mathbf{T}_{ui} &= \begin{bmatrix} \cos\ \phi_{hi} & -\sin\ \phi_{hi} \\ \sin\ \phi_{hi} & \cos\ \phi_{hi} \end{bmatrix}, \\
\mathbf{T}_{pi} &= \begin{bmatrix} \cos\ \phi_{ci} & -\sin\ \phi_{ci} \\ \sin\ \phi_{ci} & \cos\ \phi_{ci} \end{bmatrix}
\end{aligned}
$$

(A.9)

Appendix B

The bilinear shape function is shown as follows:

$$
\mathbf{N}_{ti} = \begin{bmatrix} N_{xi} \\ N_{vi} \\ N_{wi} \\ N_{\theta xi} \\ N_{\theta xi} \\ N_{\theta zi} \end{bmatrix} = \begin{bmatrix} (1 + \xi_i\xi)(1 + \eta_i\eta) \\ (1 + \xi_i\xi)(1 + \eta_i\eta) \\ (1 + \xi_i\xi)(1 + \eta_i\eta) \\ (1 + \xi_i\xi)(1 + \eta_i\eta) \\ (1 + \xi_i\xi)(1 + \eta_i\eta) \\ (1 + \xi_i\xi)(1 + \eta_i\eta) \end{bmatrix},
$$
$$
\mathbf{N}_{si} = \begin{bmatrix} N_{xi} \\ N_{vi} \\ N_{wi} \\ N_{\theta xi} \\ N_{\theta xi} \\ N_{\theta xi} \end{bmatrix} = \frac{1}{4}\begin{bmatrix} \xi_i(1 + \eta_i\eta) \\ \xi_i(1 + \eta_i\eta) \\ \xi_i(1 + \eta_i\eta) \\ \xi_i(1 + \eta_i\eta) \\ \xi_i(1 + \eta_i\eta) \\ \xi_i(1 + \eta_i\eta) \end{bmatrix}
$$

(B.1)

where
$\xi = (x - x_c)/a, \eta = (y - y_c)/b, \xi_i = x_i/|x_i|,$-
. (x_c, y_c) is the center coordinates of the element. a and b are the length and width of the element, respectively.

The generalized coordinates $\mathbf{p}$ can be transformed into unique generalized coordinates $\mathbf{q}$ with Boolean matrix $\mathbf{\Gamma}_B$:

Table 6 Main notations of the vehicle subsystem and bridge subsystem

Notations	Descriptions
M_c, M_t, M_h	Mass of car body, hanging beam and bogie
I_{cx}, I_{cy}, I_{cy}	X-inertia, Y-inertia, Z-inertia of car body
I_{tx}, I_{ty}, I_{ty}	X-inertia, Y-inertia, Z-inertia of bogie
I_{hx}, I_{hy}, I_{hy}	X-inertia, Y-inertia, Z-inertia of hanging beam
K_{sx}, K_{sy}, K_{sz},	Longitudinal, lateral and vertical stiffness of the secondary suspension, respectively
C_{sx}, C_{sy}, C_{sz},	Longitudinal, lateral and vertical damping of the secondary suspension, respectively
L_c, L_g and L_t	Longitudinal distance between center of the bogie, guiding force and diving tyre, respectively
K_{dx}, K_{rl}, K_{pt}	Longitudinal, anti-rolling and anti-pitching equivalent stiffness of four-linkage mechanical device, respectively
K_{dx}, K_{dy}, K_{dz}	Longitudinal, lateral and vertical stiffness of the driving tyre, respectively
C_{dx}, C_{dy}, C_{dz}	Longitudinal, lateral and vertical damping of the driving tyre, respectively
k_{gy}, c_{gy}	Vertical stiffness and damping of the guiding tyre, respectively
k_{dz}, c_{dz}	Vertical stiffness and damping of the driving tyre, respectively
H_{cb}	Vertical distance from the centroid of the car body to the linkage CD
H_{bt}	Vertical distance from the centroid of the bogie to the lower surface of secondary suspension
H_{hf}, H_{hr}	Vertical distance from the centroid of the hanging beam to the upper surface of secondary suspension and linkage AB AB
F_{xt}, F_{yt}, F_{zt}	Longitudinal, lateral and vertical force of the secondary suspension, respectively
F_{dcx}, M_{rr}	Longitudinal force and rolling torque of four-linkage mechanical device, respectively
F_{cpf}, F_{cpr}	Coupler force of front vehicle and rear vehicle, respectively
F_{shf}, F_{shr}	Force of front and rear shock absorbers, respectively
F_{rbl}, F_{rbr}	Force of front and rear shock absorbers, respectively
Z_b, Z_r	Vertical displacements of the bridge and driving tyre, respectively
$R_{\Delta dt}$, $R_{\Delta dt}$	Vertical deformation and rate of deformation of the driving tyre, respectively
σ_{0m}, σ_{1m}, σ_{2m}	Stiffness and damping coefficient of brush bristle
μ_c, μ_s	Static friction coefficient and kinetic friction coefficient matrix, respectively
$M^{(k)}$, $K^{(k)}$	Mass and stiffness matrix of kth substructure, respectively
$T^{(k)}$, $\Phi^{(k)}$, $\Psi^{(k)}$	Mode basis, fixed-interface normal mode and static mode of kth substructure, respectively
$\widetilde{M}^{(k)}$, $\widetilde{K}^{(k)}$	Mass and stiffness matrix of the kth reduced substructure, respectively

Table 7 Main parameter of the vehicle subsystem and bridge subsystem

Notations	Value	Unit
Mass of car body (Empty/Normal)	8000/9200	kg
Mass of bogie	2000	kg
Longitudinal spacing of bogies	5.95	m
Longitudinal spacing of guiding tyres	2.49	m
Longitudinal spacing of driving tyres	1.60	m
The lateral span of driving tyres	0.50	m
Elastic modulu	210	GPa
Density	7850	kg/m^3
Poisson ratio	0.30	–

$$\boldsymbol{\Gamma}_B = \begin{bmatrix} \mathbf{I}_{p_1} & \mathbf{0} & \mathbf{0} & & & & \\ \mathbf{0} & \mathbf{I}_{p_{t1}} & \mathbf{0} & & & & \\ \mathbf{0} & \mathbf{0} & \mathbf{I}_{b_1} & \cdots & & & \\ \mathbf{0} & \mathbf{I}_{b_{t1}} & \mathbf{0} & & & & \\ & & & & \ddots & & \\ & & & & & \mathbf{I}_{p_{tn}} & \\ & & & \cdots & & & \mathbf{I}_{p_n} \end{bmatrix} \tag{B.2}$$

where $\mathbf{I}_{pi}$ and $\mathbf{I}_{bi}$ denote the identity matrix for the internal DOFs of the track beam and pier substructure, respectively; $\mathbf{I}_{pti}$ and $\mathbf{I}_{bi}$ denote the identity matrix for the interface DOFs of the track beam and pier substructure, respectively.

Appendix C

See Table 6 and 7.

References

1. Sambaiah, K.S., Jayabarathi, T.: Optimal modeling and allocation of mixed wind and solar generation systems in electric distribution networks. IETE J. Res. **68**(6), 4129–4141 (2022)

2. Pathak, D.P., Khatod, D.K.: Development of integrated renewable energy system based on optimal operational strategy and sizing for an un-electrified remote area. IETE. J. Res. 1–20 (2021)

3. Yin, W., Mavaluru, D., Ahmed, M., Abbas, M., Darvishan, A.: Application of new multi-objective optimization algorithm for EV scheduling in smart grid through the uncertainties. J. Ambient. Intell. Humaniz. Comput. **11**, 2071–2103 (2020)

4. Behera, S., Behera, S., Barisal, A.K.: Dynamic economic emission dispatch including electric vehicles' demand management and vehicle to grid support considering physical constraints. J. Ambinet Intell. Humaniz. Comput. **14**(3), 2739–2757 (2023)

5. Dominguez, J., Campillo, J., Campo-Landines, K., Contreras-Ortiz, S.H.: Impact of emotional states on the effective range of electric vehicles. J. Ambient Intell. Humaniz. Comput. **14**(7), 9049–9058 (2023)

6. Victor, D.J., Ponnuswamy, S.: Urban Transportation: Planning, Operation and Management. Tata McGraw-Hill Education (2012)

7. Grava, S.: Urban Transportation Systems, Choices for Communities. McGraw-Hill, New York (2003)

8. Cai, C., He, Q., Zhu, S., et al.: Dynamic interaction of suspension-type monorail vehicle and bridge: numerical simulation and experiment. Mech. Syst. Signal Process. **118**(3), 388–407 (2019)

9. He, Q., Cai, C., Zhu, S., et al.: An improved dynamic model of suspended monorail train-bridge system considering a tyre model with patch contact. Mech. Syst. Signal Process. **144**(10), 106865 (2020)

10. Jiang, Y., Wu, P., Zeng, J., et al.: Multi-parameter and multi-objective optimisation of articulated monorail vehicle system dynamics using genetic algorithm. Veh. Syst. Dyn. **58**(1), 74–91 (2019)

11. Hesser, D.F., Altun, K.B.: Markert: monitoring and tracking of a suspension railway based on data-driven methods applied to inertial measurements. Mech. Syst. Signal Process. **164**, 108298 (2022)

12. Zhu, B., Zhang, C., Zhang, Z.L., et al.: Dynamic analysis of suspension-type monorail long-span cable-stayed bridge in a wind-vehicle-bridge system. Urban Rail Transit **9**(1), 19–30 (2023)

13. Sobhanam, A.P., Mary, P.M., Mariasiluvairaj, W.I., et al.: Automatic generation control using an improved artificial electric field in multi-area power system. IETE J. Res. 1–13 (2021)

14. Ma, L., Lu, Y.A.: Intelligent charging control method of shared vehicle based on MPPT algorithm in the environment of internet of things. J. Ambinet Intell. Humaniz. Comput. 1–9 (2021)

15. Verma, K., Ghosh, D., Kumar, A.: Visual tracking in unstabilized real time videos using SURF. J. Ambinet Intell. Humaniz. Comput. 1–19 (2019)

16. Lotfi, H., Ghazi, R.: Optimal participation of demand response aggregators in reconfigurable distribution system considering photovoltaic and storage units. J. Ambinet Intell. Humaniz. Comput. **12**, 2233–2255 (2021)

17. Yang, Y.B., Wu, Y.S.: A versatile element for analyzing vehicle–bridge interaction response. Eng. Struct. **23**(5), 452–469 (2001)

18. Law, S.S., Zhu, X.Q.: Bridge dynamic responses due to road surface roughness and braking of vehicle. J. Sound Vib. **282**(3–5), 805–830 (2005)

19. Ju, S.H., Lin, H.T.: A finite element model of vehicle–bridge interaction considering braking and acceleration. J. Sound Vib. **303**(1), 46–57 (2007)

20. Zhai, W., Han, Z., Chen, Z.L., et al.: Train–track–bridge dynamic interaction: a state-of-the-art review. Veh. Syst. Dyn. **57**(7), 984–1027 (2019)

21. Yang, Y.B., Wang, Z.L., Shi, K., et al.: State-of-the-art of the vehicle-based methods for detecting the various properties of highway bridges and railway tracks. Int. J. Struct. Stab. Dyn. **20**(13), 2041004 (2020)

22. Lei, S.M., Ge, Y.J., Li, Q., et al.: Frequency-domain method for non-stationary stochastic vibrations of train-bridge coupled system with time-varying characteristics. Mech. Syst. Signal Process. **183**, 109637 (2023)

23. Zhou, S.H., Song, G.Q., Ren, Z.H., et al.: Nonlinear dynamic analysis of a parametrically excited vehicle–bridge interaction system. Nonlinear Dyn. **88**(3), 2139–2159 (2017)

24. Antolín, P., Zhang, N., Goicolea, J.M., et al.: Consideration of nonlinear wheel–rail contact forces for dynamic vehicle–bridge interaction in high-speed railways. J. Sound Vib. **332**(5), 1231–1251 (2013)

25. Montenegro, P.A., Calçada, R., Vila Pouca, N., et al.: Running safety assessment of trains moving over bridges subjected to moderate earthquake. Earthq. Eng. Struct. D **45**(3), 483–504 (2016)

26. Tang, S., Liu, G., Lin, Z., Li, X.: Multi-station test scheduling optimization method for industrial robot servo system. J. Ambinet Intell. Humaniz. Comput. 1–17 (2022)

27. Din, A.F.U., Mir, I., Gul, F., Akhtar, S.: Development of reinforced learning based non-linear controller for unmanned aerial vehicle. J. Ambinet Intell. Humaniz. Comput. **14**(4), 4005–4022 (2023)

28. Taimoor, M., Aijun, L., Samiuddin, M.: Sliding mode learning algorithm based adaptive neural observer strategy for fault estimation, detection and neural controller of an aircraft. J. Ambinet Intell. Humaniz. Comput. **12**, 2547–2571 (2021)

29. Li, T.Y., Song, Y.H., Xia, X.T.: Research on remote control algorithm for parallel implicit domain robot patrol inspection on 3D unstructured grid. J. Ambinet Intell. Humaniz. Comput. **11**, 6337–6347 (2020)

30. John, F. L., Dogra, D.: Application research of network learning algorithm based on neural network disturbance

compensation in satellite attitude control. J. Ambinet Intell. Humaniz. Comput. 1–8 (2022)

31. Yang, Y., He, Q., Cai, C., et al.: Coupled vibration analysis of suspended monorail train and curved bridge considering nonlinear wheel-track contact relation. Veh. Syst. Dyn. **60**(8), 2658–2685 (2021)

32. Periyanayagi, S., Pazhani, A.A.J., Sumathy, V.: Enhanced humanoid assisted human interaction model based on linear structural modeling for knowledge representation. J. Ambinet Intell. Humaniz. Comput. **11**(12), 6307–6318 (2020)

33. Canché, M., Ochoa, S.F., Perovich, D., Gutierrez, F.J.: Analysis of notations for modeling user interaction scenarios in ubiquitous collaborative systems. J. Ambinet Intell. Humaniz. Comput. 1–13 (2019)

34. Kobylarz, J., Bird, J.J., Faria, D.R., Ribeiro, E.P., Ekárt, A.: Thumbs up, thumbs down: non-verbal human-robot interaction through real-time EMG classification via inductive and supervised transductive transfer learning. J. Ambinet Intell. Humaniz. Comput. **11**, 6021–6031 (2020)

35. Nota, G., Aiello, R.: The interaction type approach to relationships management. J. Ambinet Intell. Humaniz. Comput. **10**, 239–253 (2019)

36. Zhai, Z.H., Cai, C.B., Zhu, S.Y.: Implementation of Timoshenko curved beam into traintrack-bridge dynamics modelling. Int. J. Mech. Sci. **247**, 108158 (2023)

37. Yang, Y.B., Chang, C.H., Yau, J.D.: An element for analysing vehicle–bridge systems considering vehicle's pitching effect. Int. J. Numer. Meth. Eng. **46**, 1031–1047 (1999)

38. Au, F.T.K., Wang, J.J., Cheung, Y.K.: Impact study of cable-stayed bridge under railway traffic using various models. J. Sound Vib. **240**(3), 447–465 (2001)

39. Zhang, Y., Zhao, H., Lie, S.T.: A nonlinear multi-spring tyre model for dynamic analysis of vehicle–bridge interaction system considering separation and road roughness. J. Sound Vib. **436**, 112–137 (2018)

40. Deng, L., Cao, R., Wang, W., et al.: A multi-point tyre model for studying bridge-vehicle coupled vibration. Int. J. Struct. Stab. Dyn. **16**(8), 1550047 (2016)

41. Kim, S.P., Nikravesh, E., Gim, G.: A two-dimensional tyre model on uneven roads for vehicle dynamic simulation. Veh. Syst. Dyn. **10**, 46 (2008)

42. Pacejka, H.B., Besselink, I.J.M.: Magic formula tyre model with transient properties. Veh. Syst. Dyn. **27**(1), 234–249 (1997)

43. Gipser, M.: Ftire: a physically based application-oriented tyre model for use with detailed mbs and finite-element suspension models. Veh. Syst. Dyn. **43**(1), 76–91 (2005)

44. Zegelaar, P.W.A., Gong, S., Pacejka, H.B.: Tyre models for the study of in-plane dynamics. Veh. Syst. Dyn. **23**(1), 578–590 (1994)

45. López, A., Olazagoitia, J.L., Moriano, C., et al.: Nonlinear optimization of a new polynomial tyre model. Nonlinear Dyn. **78**(4), 2941–2958 (2014)

46. Zhuang, Y., Song, Z., Gao, X., et al.: A combined-slip physical tire model based on the vector distribution considering tire anisotropic stiffness. Nonlinear Dyn. **108**(4), 2961–2976 (2022)

47. Marques, F., Woliński, Ł, Wojtyra, M., et al.: An investigation of a novel LuGre-based friction force model. Mech. Mach. Theory **166**, 104493 (2021)

48. Romano, L., Bruzelius, F., Jacobson, B.: An extended LuGre-brush tyre model for large camber angles and turning speeds. Veh. Syst. Dyn. https://doi.org/10.1080/00423114.2022.2086887

49. Bathe, K.J., Dvorkin, E.N.: A four-node plate bending element based on Mindlin/Reissner plate theory and a mixed interpolation. Int. J. Numer. Methods Eng. **21**(2), 367–383 (1985)

50. Craig, R.R., Bampton, C.C.: Coupling of substructures for dynamic analyses. AIAA J. **6**(7), 1313–1319 (1968)

51. Suarez, L.E., Singh, M.P.: Modal synthesis method for general dynamic systems. J. Eng. Mech. **118**(7), 1488–1503 (1992)

52. Agabein, M.E.: The effect of various damping assumptions on the dynamic response of structures. Bull. Int. Inst. Seismol. Earthq. Eng. **8**(1), 217–236 (1971)

53. Zhang, W., Lv, S., Ni, Y.: Parametric aeroelastic modeling based on component modal synthesis and stability analysis for horizontally folding wing with hinge joints. Nonlinear Dyn. **92**, 169–179 (2018)

54. Lanczos, C., Res, J.: Nat. Bur. Stand. **45**, 255 (1950)

55. Zhou, Y., Zhang, Y., Zeng, W., et al.: Fast modification-aimed stress modal analysis of thin plates with holes/notches. Eng. Struct. **238**(7), 112248 (2021)

56. Wang, T., Celik, O., Catbas, F.N., et al.: A frequency and spatial domain decomposition method for operational strain modal analysis and its application. Eng. Struct. **27**(5), 62–66 (2016)

57. Zhai, W.M.: Two simple fast integration methods for large-scale dynamic problems in engineering. Int. J. Numer. Meth. Eng. **39**(24), 4199–4214 (1996)

58. Newmark, N.M.: A method of computation for structural dynamics. Proc. ASCE. **85**(1), 67–94 (1959)

59. DBJ51/T 099: Standard for design of suspended monorail transit. Southwest Jiaotong University Press, Chengdu (2018)

60. Li, J., Zhu, X., Law, S.: Time-varying characteristics of bridges under the passage of vehicles using synchroextracting transform. Mech. Syst. Signal Process. **140**(6), 106727.1-106727.19 (2020)

61. ISO 2631-1: Mechanical vibration and shock—evaluation of human exposure to whole-body vibration—art 1: general requirements, Switzerland (1997)